Eastern Pacific Hurricanes Jimena of 1991 and Olivia of 1994: The Effect of Vertical Shear on Structure and Intensity

M. L. BLACK, J. F. GAMACHE, F. D. MARKS JR., C. E. SAMSURY,* AND H. E. WILLOUGHBY

NOAA/AOML/Hurricane Research Division, Miami, Florida

(Manuscript received 16 May 2001, in final form 21 January 2002)

ABSTRACT

Shear is a key inhibitor of tropical cyclone intensification. Although its signature is readily recognized in satellite imagery and theoretical or modeling studies provide some insight, detailed observations have been limited. Airborne radar and in situ observations in Hurricanes Jimena of 1991 and Olivia of 1994 are a step toward better understanding. Each storm was observed on two consecutive days. Initially, both had small eyes, 16–18-km radius, and maximum winds of ~57 m s^{-1} over sea surface temperatures (SST) >28°C in easterly environmental shear. Jimena maintained constant intensity or weakened gradually for 2 days in 13–20 m s^{-1} easterly shear. Olivia intensified in 8 m s^{-1} shear on the first day. Overnight, the shear diminished to reverse and became westerly. On the second day, Olivia weakened as the shear increased to >15 m s^{-1} from the west, the storm moved over cooler SST, and became surrounded by dryer air. As convection weakened and the outer rainbands ceased to be effective barriers, relative flow due to the environmental shear penetrated more deeply into the vortex core.

In both storms, shear controlled the convective structure. Convection organized itself into axisymmetric rings as Olivia intensified in weak shear. When both storms encountered stronger shear, radar reflectivity and vertical motion had strong wavenumber-1 components. Highest reflectivity lay generally to the left of the shear. Most radar echoes and updrafts formed in the downshear quadrant of the storm and advected around the eye with 60%–80% of the swirling wind, consistent with vortex Rossby wave propagation. The buoyant updrafts accelerated and reflectivity increased as they passed through the left-of-shear semicircle. On the upshear side, the updrafts rose through the 0°C isotherm, and hydrometeors fell out or froze. Reflectivity declined as the echoes transformed into lower-tropospheric downdrafts overlain by glaciated upper-tropospheric updrafts in the right-of-shear semicircle.

In relatively weak shear, clusters of echoes could be tracked completely around the eye. Each time the clusters passed through the downshear and left-of-shear quadrants, new echoes would form. In strong shear, all echoes were short lived, and none could be tracked around the eye. Echoes appeared downshear of the center and completed their life cycles on the left side of the shear vector where the composite reflectivities were greatest.

1. Introduction

Eastern Pacific Hurricanes Jimena and Olivia (Fig. 1) constitute a controlled experiment in the effects of vertical shear and sea surface temperature (SST) on hurricane convective structure and intensity. Both occurred in late September, Jimena in 1991 and Olivia in 1994. Jimena was observed by NOAA's WP-3D research aircraft, *N42RF* and *N43RF*, on the first of two successive days and by *N43RF* alone on the second day. While monitored by the aircraft, Jimena moved westward in nearly constant easterly shear over warm water. The two aircraft observed Olivia on both days. Olivia, too, was initially in easterly shear over warm water. The shear decreased and then became stronger again from the west-northwest as Olivia moved northward over cooler SST. The differences in structure and intensity under these changing conditions provide insight into environmental forcing of hurricanes.

Three factors determine tropical cyclone structure and intensity: the cyclones' internal dynamics, the oceanic energy source, and lateral forcing by the surrounding atmosphere. In the convective ring model (Willoughby 1990), axisymmetric convection is localized by frictional convergence near the radius of maximum wind (RMW). Diabatically driven angular momentum convergence above the frictional boundary layer accelerates the swirling wind and causes contraction of the eye. Pressure falls, largely concentrated inside the RMW, stem from gradient-wind adjustment of the mass to the increasing wind. This model is well described by strictly axisymmetric solutions of the Sawyer–Eliassen equation (Smith 1981; Shapiro and Willoughby 1982; Schubert and Hack 1982).

* Current affiliation: The Weather Channel, Atlanta, Georgia.

Corresponding author address: Dr. H. E. Willoughby, NOAA/AOML/Hurricane Research Division, 4301 Rickenbacker Cswy., Miami, FL 33149.
E-mail: hugh.willoughby@noaa.gov

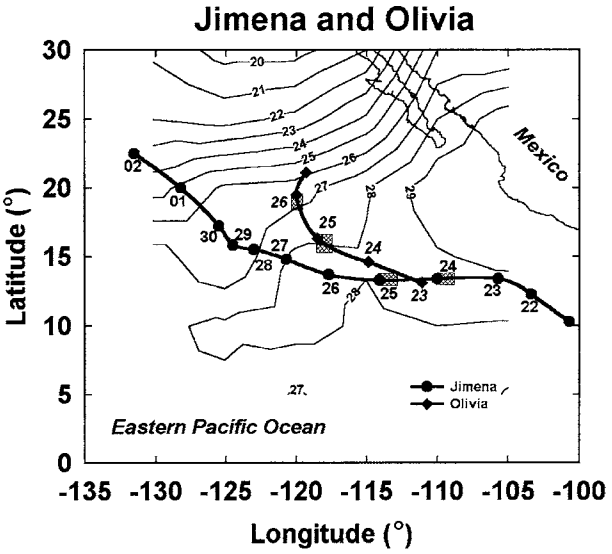

FIG. 1. The tracks of eastern North Pacific Hurricanes Jimena (circles show 0000 UTC position on the date indicated by plain numbers) during Sep 1991, and Olivia (diamonds, italic numbers) during Sep 1994, superimposed upon isotherms of SST for 25 Sep 1994 from the OTIS (Optimum Thermal Interpolation System) analysis prepared by the U. S. Navy's Fleet Numerical Meteorology and Oceanography Center. Shaded boxes indicate the times of detailed aircraft observation. The 26°C isotherm marks the Cabo San Lucas oceanic front. Contemporary Reynolds SST for Jimena have a similar pattern of isotherms, but are a fraction of a degree cooler.

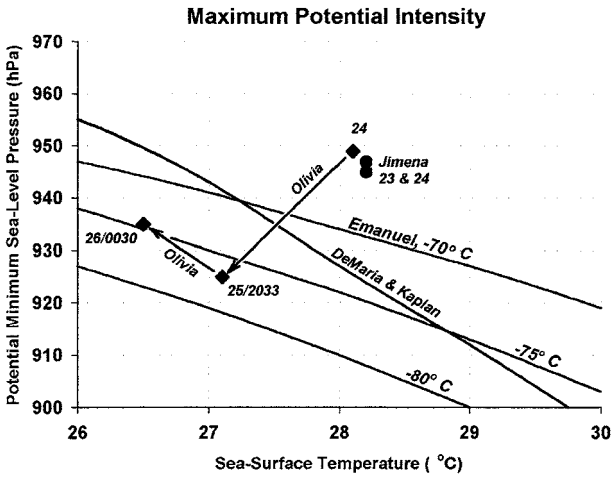

FIG. 2. MPI as a function of SST based upon Emanuel's thermodynamic argument for tropopause temperatures of −70°, −75°, and −80°C, and upon DeMaria and Kaplan's census of most-intense Atlantic hurricanes observed for each SST. Superimposed on this diagram are climatological or preexistent SST and min sea level pressures for Hurricanes Jimena and Olivia indicated as in Fig. 1 by diamonds and circles. Arrows show the changes in central pressure and SST during the time that the hurricanes were obs. Jimena remained in a nearly steady state, while Olivia strengthened and then weakened in response to evolving environmental shear and SST.

The mirror image of convective-ring intensification is vortex spindown (Eliassen and Lystad 1977) in which frictionally driven convergence causes ascent at the top of the boundary layer, which compresses the vortex tubes just above the boundary layer and induces outflow that reduces the low-level swirling wind. Reasor et al. (2000) apply this idea successfully to the second day of Olivia observations. Recent results suggest that axisymmetric response to heating, or lack of heating, is not the whole story. Potential vorticity production by heating in individual convective cells may excite vortex Rossby waves. In adiabatic models, the waves support a low-level eddy convergence of angular momentum that would reinforce the heating-induced axisymmetric convergence in a diabatic model (Montgomery and Kallenbach 1997; Montgomery and Enagonio 1998). Although Reasor et al. (2000) also examined the second day of Olivia in this context with encouraging results, this effect does not appear to be dominant.

In contrast with the Sawyer–Eliassen treatment of convective heating as an imposed buoyancy source, a more thermodynamic approach (Emanuel 1986) models tropical cyclones as heat engines in which moist enthalpy and angular momentum are state variables linked through the thermal-wind relation. In a later version of this theory (Emanuel 1988, 1991), work done against surface friction balances the energy released as humid boundary layer air rises moist adiabatically to the cold upper troposphere. The heat engine's warm reservoir is nearly in equilibrium with the sea surface at ~300 K and the cold reservoir is near the tropical tropopause at ~200 K. The thermodynamically determined equilibrium central pressure, or maximum potential intensity (MPI), is thus a function of both SST and tropopause temperature. Tabulation of the most intense Atlantic hurricanes observed for a given SST (DeMaria and Kaplan 1994) yields MPIs consistent with the thermodynamic formulation (Fig. 2)—particularly so when one considers the climatological correlation of a higher and colder tropopause with warmer SST.

Most hurricanes fail to reach their MPI, primarily because of storm-induced cooling of the sea or the inhibiting effects of shear. Shears greater than a threshold of 12.5 m s^{-1} prevent development of tropical cyclones in the western North Pacific (Zehr 1992). Conventional wisdom points to vertical shear of the environmental wind as the most widespread atmospheric influence on tropical cyclone intensity. A contrary view accepts shear as an inhibitor of *formation,* but hypothesizes weakening of mature tropical cyclones primarily when shear combines with weak thermodynamic forcing (e.g., Holland 1997). In the earliest explanation (Simpson and Riehl 1958), shear was thought to inhibit intensification because differential advection separated the upper warm anomaly from the low-level circulation. Theoretical work (Jones 1995) suggests that the vortex initially tilts downshear after a shear flow is imposed. The downward projection of the upper circulation and the upward projection of the lower circulation cause the centers to circle cyclonically around the midlevel center. Eventually, the rotation of the tilted axis stops, but the magnitude of

the tilt continues to increase. It is argued that these motions act to keep the vortex together through cancellation of vertical differences of environmental advection. In adiabatic vortex flow, the mean axisymmetric circulation follows the sloping environmental potential temperature surfaces that maintain the environmental shear in thermal-wind balance. This effect results in asymmetric ascent on the downshear side and descent on the upshear side (Raymond 1992; Raymond and Jiang 1990). Similar patterns occur in models that incorporate convection (e.g., Wu and Emanuel 1993; Flatau et al. 1994). Vertical advection by this asymmetric secondary flow acts to reduce the tilt and helps to maintain the integrity of the vortex. The asymmetric distribution of stability as a result of the tilt may also have a role in the asymmetric distribution of convection (DeMaria 1996).

Full physics tropical cyclone models produce results consistent with the foregoing description. Peng et al. (1999) used a 0.5°-resolution, 16-level model with parameterized convection. They noted fastest intensification and greatest ultimate intensity on an f plane with no environmental flow. Introduction of either the β effect or a uniform environmental flow slowed intensification and weakened the storm by forcing asymmetric convection, apparently through enhanced asymmetric surface fluxes. A 5 m s^{-1} westerly flow that partially cancelled the β effect allowed somewhat greater intensity than the other cases with environmental flows. Earlier work with the Geophysical Fluid Dynamics Laboratory (GFDL) hurricane model (Bender 1997) established the inhibiting effect of asymmetric convection. In uniform along-track shear, differential advection of the mean-vortex vorticity by the relative flow due to the shear produced low-level convergence overlain by upper-level divergence on the downshear side of the eyewall and low-level divergence overlain by upper-level convergence on the upshear side. As the mean swirling flow blew through this convergence dipole, water condensed in the ascent on the downshear side. Hydrometeors advected through the left-of-shear semicircle and had largely rained out by the time the flow reached the forced descent on the upshear side. Frank and Ritchie (1999) used a 15-km resolution version of the fifth-generation Pennsylvania State University–National Center for Atmospheric Research Mesoscale Model (MM5) to show that forced ascent in the dry model actually began upstream (i.e., to the right) of the downshear direction. In a moist model, condensational heating accelerated the updrafts so that the strongest vertical velocities lay downstream (i.e., to the left) of the downshear direction. Shear controlled the reflectivity structure to a greater extent than did surface friction. As in the other models, hydrometeors advected through the left-of-shear semicircle producing the greatest reflectivity and rainfall rates there. Additional simulations using a 5-km-resolution version of MM5 with resolved convection produced similar patterns by modulation of the life cycles of convection elements relative to the shear vector (Frank and Ritchie 2001). The simulated hurricane reached steady-state potential intensities weaker than the MPI for the fixed 28.5°C SST.

Another potential atmospheric interaction is intensification triggered by upper-level angular momentum fluxes (e.g., Molinari et al. 1998). A statistically significant climatological correlation is present, but only after account is taken of the simultaneous effects of shear and SST (DeMaria et al. 1993). Sometimes combined atmospheric and oceanic forcing can produce spectacular fluctuations of intensity, as in Hurricane Opal of 1995 (Bosart et al. 2000; Hong et al. 2000; Shay et al. 2000). Although it is not possible to discount a role for eddy momentum fluxes in Jimena's and Olivia's evolution, changes in shear and SST appear to be dominant.

a. Hurricane Jimena

The system that later became Hurricane Jimena (Rappaport and Mayfield 1992) began as a wave over Africa in early September 1991. It spawned Atlantic Tropical Storm Danny, but split and weakened during passage over Central America. The southern part moved northwestward in the eastern Pacific (Fig. 1). It reintensified to a depression on 20 September, became Tropical Storm Jimena on 21 September, then intensified rapidly on 22 September to become a hurricane, and turned due west. The research flights in Jimena staged from Puerto Vallarta, Mexico, on 23 and 24 September. Between 1200 and 1800 UTC on 24 September, Jimena reached maximum intensity, officially 59 m s^{-1} wind at 945-hPa sea level pressure measured by dropsonde (Willoughby 1998). Although Jimena remained over 28°C SST,[1] warm enough to sustain 925–930 hPa on DeMaria and Kaplan's MPI curve (Fig. 2), moderate (13–15 m s^{-1}) easterly shear caused constant intensity weaker than the MPI, or perhaps gradual weakening. Subsequently, the storm weakened and became disorganized as it continued to move westward. On 30 September it turned northward into stronger southwesterly shear over colder water. It finally dissipated in early October.

b. Hurricane Olivia

Hurricane Olivia (Pasch and Mayfield 1996) began on 18 September 1994 as a disturbance at 10°N on the intertropical convergence zone south of Mexico. It traveled toward the west-northwest (Fig. 1), becoming a tropical depression at 0600 UTC on 22 September, a tropical storm by 1800 UTC, and a hurricane by 0600 UTC on 24 September. By 1800 UTC on 24 September, satellite estimates indicated 49 m s^{-1} winds, but airborne Doppler radar analyses showed 68 m s^{-1} winds at 1-

[1] Reynolds SST (Reynolds and Smith 1994) from the NOAA-CIRIES, Climate Diagnostics Center Web site http://www.cdc.noaa.gov.

km altitude. Thus, Hurricane Olivia had intensified on 24 September over SST able to sustain MPI $<$ 924 hPa on DeMaria and Kaplan's curve (Fig. 2), and continued to do so during the first research mission, despite some easterly shear. The only eye sounding on 24 September had 949-hPa surface pressure (Willoughby 1998). During and after the flights, Olivia moved around a deep-layer-mean anticyclone to assume a northwestward track. Shortly thereafter, Olivia's motion was influenced by a midtropospheric cyclone a few hundred kilometers west of the California–Mexico border.

On 25 September, the second day of aircraft operations, the hurricane moved northward across the strong SST gradient. Aircraft fixes defined a track just east of north. Peak intensity apparently occurred overnight between the flights. The satellite intensity estimate for 1200 UTC on 25 September was 923 mb, now 20 hPa below the MPI for the preexistent SST. It compares favorably with the lowest pressure measured by dropsonde, 925 hPa at 2106 UTC (Willoughby 1998). The final dropsonde central pressure, near the end of the second day's operations, was 937 hPa at 2349 UTC—still below the 950 hPa MPI for the cooler SST (Fig. 2). Although Olivia weakened throughout the 4 h that the airplanes were in the storm, they apparently arrived before it had weakened appreciably from its maximum intensity.

Satellite observations indicate that, as Olivia encountered the midtropospheric cyclone overnight, the easterly shear from 24 September had decreased. By the time the aircraft finally left the storm just after 0000 UTC on 26 September, the shear had increased from the west to become nearly as strong as in Jimena, but from west-northwest. Maximum winds estimated by satellite decreased to 51 m s^{-1} by late on 26 September. The storm made a slow loop, weakened to a depression by 1200 UTC on 28 September, and dissipated the next day.

2. Operations

a. Aircraft instrumentation

Flight-level meteorological instruments on the NOAA WP-3Ds have remained stable since Jorgensen (1984a) described them. Thermodynamic variables—temperature, humidity, static pressure, and dynamic pressure—are recorded at 1 Hz. The wind is determined as the difference between the true airspeed vector and the actual motion in space measured by GPS and inertial navigation. Analysis of hurricanes' thermodynamic and kinematic data focuses on observations made during radial penetrations or exits of the eye. The analysis begins with construction of the cyclone track by the method of Willoughby and Chelmow (1982) and interpolation of the observations onto a 0.5-km radial grid that moves with the vortex, as described in Willoughby et al. (1982, 1984). Winds are transformed into storm-relative coordinates by subtraction of the vortex motion. The result of the analysis is a series of 100–150-km-long radial profiles that characterize the vortex structure at flight level.

The WP-3Ds' lower-fuselage radar operates in C band (5-cm wavelength). It scans in a plan position indicator (PPI) mode—360° horizontal planes to map the horizontal distribution of reflectivity. Returned power, upon which reflectivity estimates are based, is diminished by attenuation and partial beam filling, which become more severe with increasing range. Analysis of aircraft radar data can compensate for these effects through reflectivity time compositing on a 1-km grid that moves with the vortex center (Marks 1985). As the aircraft flies through the storm, each grid point retains its highest observed reflectivity. At some time during the ~0.5 h required to traverse the vortex, the aircraft passes close enough to most grid points for attenuation and beam filling to be unimportant. The result—obtained at the expense of blurring rapidly evolving features—is reliable estimation of the spatial distribution of reflectivity.

In addition to the PPI radars, both aircraft carry X band (3 cm) Doppler radars (Jorgensen et al. 1983). Their beams scan in a vertical plane as antennas in the tail of the airplane rotate around a horizontal axis (Gamache et al. 1995). The plane of rotation can be tilted as much as 25° forward or aft of perpendicular to the fuselage. When the drift angle required to achieve a desired track over the ground is $<$25°, the antenna scans in a plane containing zenith and nadir and perpendicular to the aircraft track in the horizontal. An advantage of perpendicular scanning is acquisition of vertical incidence (VI) profiles in which the vertical beams are combined into cross sections of vertical motions and reflectivity (Fig. 3a). In an alternate mode, the antenna scans in cones a fixed number of degrees forward or aft of perpendicular to the fuselage on alternate sweeps (Fig. 3b). This technique is called the Fore/Aft Scanning Technique, (FAST; Jorgensen et al. 1996). In FAST, intersections between the forward-scanning beams and aft-scanning beams originating at different times provide two independent perspectives needed to determine the horizontal wind. During 1991, the year of Jimena, the Electra Doppler Radar ELDORA/ASTRAIA dual-beam antenna (Hildebrand et al. 1994) was installed on *N43RF* to accomplish the same effect as FAST using a pair of fixed antennas that scanned continuously 19.5° forward or aft.

When a radar with a single antenna scans perpendicular to the track, the airplane must either turn to observe the same volume from a different perspective or operate in conjunction with a second airplane flying an intersecting perpendicular track (Fig. 3c). As discussed in Jorgensen et al. (1983), dual Doppler winds, combined with mass continuity, provide enough information to reconstruct the three-dimensional wind field within the volume observed. True airborne dual-Doppler and vertical incidence radar observations were the primary ra-

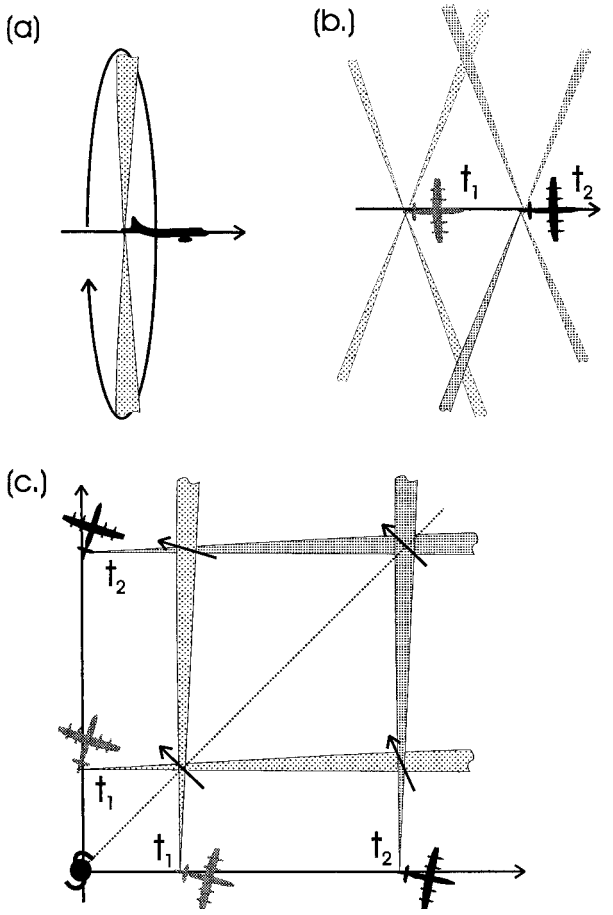

FIG. 3. Airborne Doppler radar geometry: The antenna rotates about a horizontal axis aligned with the aircraft fuselage and can be set to scan at an angle to the axis. Doppler radial winds from at least two perspectives are required to determine the vector wind. When the radar points vertically, it can measure the vertical air motion directly after correction for hydrometeor fall speed. Some scanning strategies are: (a) Vertical incidence in which the radar scans in a plane normal to the aircraft track. Vertical cross sections of reflectivity and vertical motions along the flight track are constructed by combining the radials that point at zenith and nadir. (b) Dual-beam antenna or forward and aft scanning with intersecting beams originating at different times on the straight track of a single airplane. (c) True dual Doppler in which two aircraft fly along intersecting perpendicular tracks such that they pass through the hurricane center at different altitudes. The observations are simultaneous along the diagonal bisecting the tracks. Off the diagonal, their times may differ by as much as 10 min. In (b) and (c), two observations of the same vol determine the wind projected on an inclined plane defined by the intersecting paths of the Doppler beams from the antennas to the volume obs.

dar techniques used to study Jimena and Olivia. The key application of dual-Doppler analysis for this paper was construction of ''environmental'' hodographs. The Doppler winds were resolved into Cartesian components and averaged on horizontal planes over an annulus that encircled the eye between 20- and 30-km radius to estimate the vertically shearing, but horizontally uniform, flow in which the eye and eyewall were embedded (Marks et al. 1992).

Vertical incidence radar observations consist of Doppler velocities and reflectivities recorded as the tail radar pointed toward the zenith and nadir on each sweep. The WP-3Ds' true air speeds and antenna rotation speed produce a horizontal resolution of ~750 m along the aircraft track, and the data are here averaged to 300-m vertical bins. Each analysis column may extend from just above the sea surface to as high as 15-km altitude, dependent upon the vertical distribution of radar scatterers. Hydrometeor fall speeds, based upon radar reflectivity and air density, and the vertical motions of the aircraft are removed from the raw Doppler radial velocities to estimate the vertical winds (Marks and Houze 1987; Black et al. 1994; Black et al. 1996). Long-term experience with the tail radars indicates that they have an unexplained loss of power. Addition of 7 dB(Z) to the reflectivities measured with these radars makes them consistent with those measured by the PPI radar. Inasmuch as the origin and exact magnitude of the correction are uncertain, we present uncorrected tail radar reflectivities here.

b. Eyewall evolution experiment

The objective of the research missions described here was to study the convective and vortex-scale evolution of hurricanes with airborne Doppler radar. The flight plans were variations on the true dual-Doppler theme shown in Fig. 3c. After each set of simultaneous crossing tracks, the airplanes flew downwind for 45° of azimuth relative to the storm center and then back across the center. On the next iteration, after another 45° rotation, the original pattern repeated with each airplane flying the other's former track, as shown in Fig. 2 of Gamache et al. (1995). Beam geometry and the requirement for near simultaneity limited effective Doppler range to 40 km and the time window available to complete each pair of traverses to 12–20 min.

Except in Jimena, when the dual-beam antenna was installed on *N43RF*, both antennas scanned perpendicular to the flight track as the airplanes flew radially across the storm. Precise navigation and coordination between the aircraft were essential. The observations obtained during each pair of crossings were: data to support synthesis of Doppler winds wherever radar scatterers were present, a PPI composite of radar reflectivity, VI cross sections of convective structure, and flight-level measurements at two altitudes, generally ~1 km apart. All told, the data from three sorties into Jimena produced four coordinated, dual-aircraft traverses and five single-aircraft traverses with the dual-beam antenna. The four sorties into Olivia produced 15 pairs of coordinated, dual-aircraft traverses.

3. Hurricane Jimena

At 1740 UTC on 23 September 1991, *N42RF* and *N43RF* took off from Puerto Vallarta, Mexico, to study

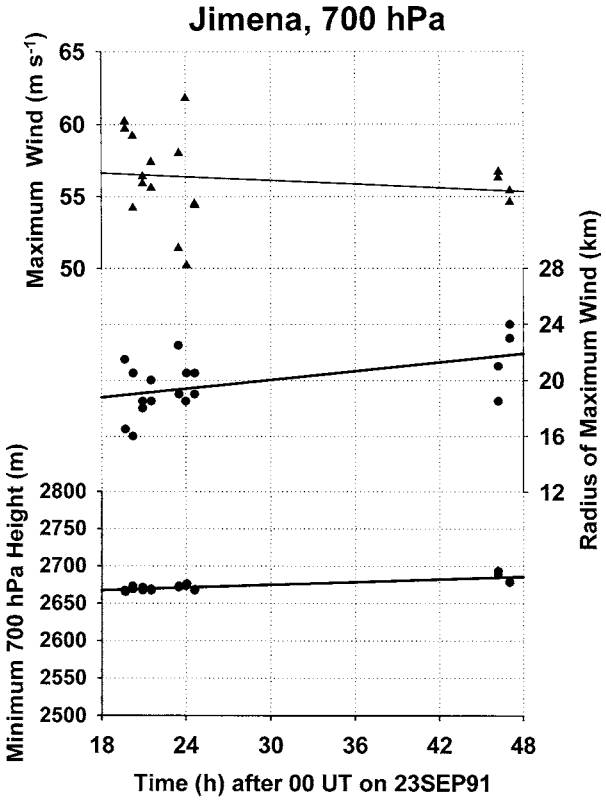

FIG. 4. Obs max wind, radius of max wind, and height of the 700-hPa surface obs in Hurricane Jimena on 23 and 24 Sep 1991. Lines are least squares fits to the observations.

Hurricane Jimena, 890 km to the SSW. An important objective was coordinated dual-Doppler traverses as shown in Fig. 3c. The aircraft started their flight patterns at approximately 1930 UTC with fuel to remain on station for 5 h with *N43RF* at 1.5-km radar altitude and *N42RF* at 3.0 km. At 2030 UTC after two penetrations, both aircraft climbed—*N43RF* to 3.0 km and *N42RF* to 4.5 km. After a total of four traverses by both aircraft, *N42RF* had an engine failure and returned to Puerto Vallarta. *N43RF* completed its pattern, flew two complete circumnavigations of the eye and then three more radial penetrations by itself. The mechanical problems meant that only *N43RF* returned to Jimena on 24 September. Although aircraft duration in the storm was limited to 3.5 h and much of this mission focused on other priorities, *N43RF* completed two passes across the storm center at 3-km altitude.

Figure 4 summarizes Jimena's history based upon flight-level data at 700 hPa. It shows changes over time of maximum wind, RMW, and height of the 700-hPa surface observed each time the aircraft traversed the eye. Transient convective asymmetries made the individual values highly variable. Although all three quantities changed in a way consistent with slow weakening, there is so much scatter that it is difficult to distinguish between weakening and constant intensity. Linear trends fitted to the data show that between the first penetration on the first day and the last exit on the second, the maximum wind decreased from 57 m s^{-1} to 55 m s^{-1}; the RMW increased from 18 to 22.5 km; and the 700-hPa height rose from 2665 m to 2685 m. Thus, the storm showed either gradual weakening or constant intensity throughout the time the aircraft monitored it, even though it remained over analyzed SST $>$ 28°C that could support MPI of 915–925 hPa.

The storm-relative hodograph (Fig. 5a) of the wind in which the vortex core was embedded on the 23d may explain the lack of intensification. Experience with hodographs prepared by averaging Cartesian Doppler winds (Marks et al. 1992) indicates that they tend to be consistent with the synoptically analyzed environmental flow (Franklin et al. 1993), but a one-to-one correspondence remains to be demonstrated. In this instance, the mean environmental wind was from slightly south of due east at 8 m s^{-1}, compared with a vortex motion from a bit north of due east (i.e., toward 265°) at 5.5 m s^{-1}. The hodograph shows that most of the shear was due to changes in speed with some veering of direction. The maximum shear was 20 m s^{-1} between 1- and 10-km altitude. Environmental flow relative to the storm varied from ~8 m s^{-1} from northwest toward southeast at 0.5 km to 12 m s^{-1} from southeast toward the northwest at 10 km. Above that level, the relative flow veered by about 30° and decreased to 10 m s^{-1}. The maximum shear was stronger than Zehr's (1992) threshold for tropical cyclone formation. It was apparently also strong enough to interfere with intensification of a 57 m s^{-1} hurricane over 28°C water.

The PPI radar composite for 1931–1951 UTC on 23 September (Fig. 5b) shows a partial principal band (Willoughby et al. 1984) that wrapped completely around the vortex from east through north, west, and south to join the eyewall on the northwest side. The horizontal distribution of reflectivity in Jimena's eyewall was asymmetric. In the southwestern semicircle of the eyewall, to the left of the shear vector, the reflectivity was $>$40 dBZ with peak values $>$45 dBZ, but the northeastern half, to the right of the shear, contained no reflectivities $>$35 dBZ.

Although this asymmetry with respect to the shear vector persisted throughout the time the aircraft operated in Jimena, it was not a steady pattern. It was, instead, a superposition of radar echoes that formed near the downshear side and advected cyclonically around the vortex. The semicircle to the left of the shear contained strongly precipitating echoes with high radar reflectivity in the lower troposphere. Jorgensen et al. (1985) showed that vertical motions in hurricanes are relatively weak. Consequently, collision–coalescence has time to generate warm rain that falls out of the updrafts in a few minutes. Similarly, ice multiplication completely glaciates most convective elements so that reflectivity decreases abruptly above the 0°C isotherm. Convection observed in Jimena was consistent with this explanation.

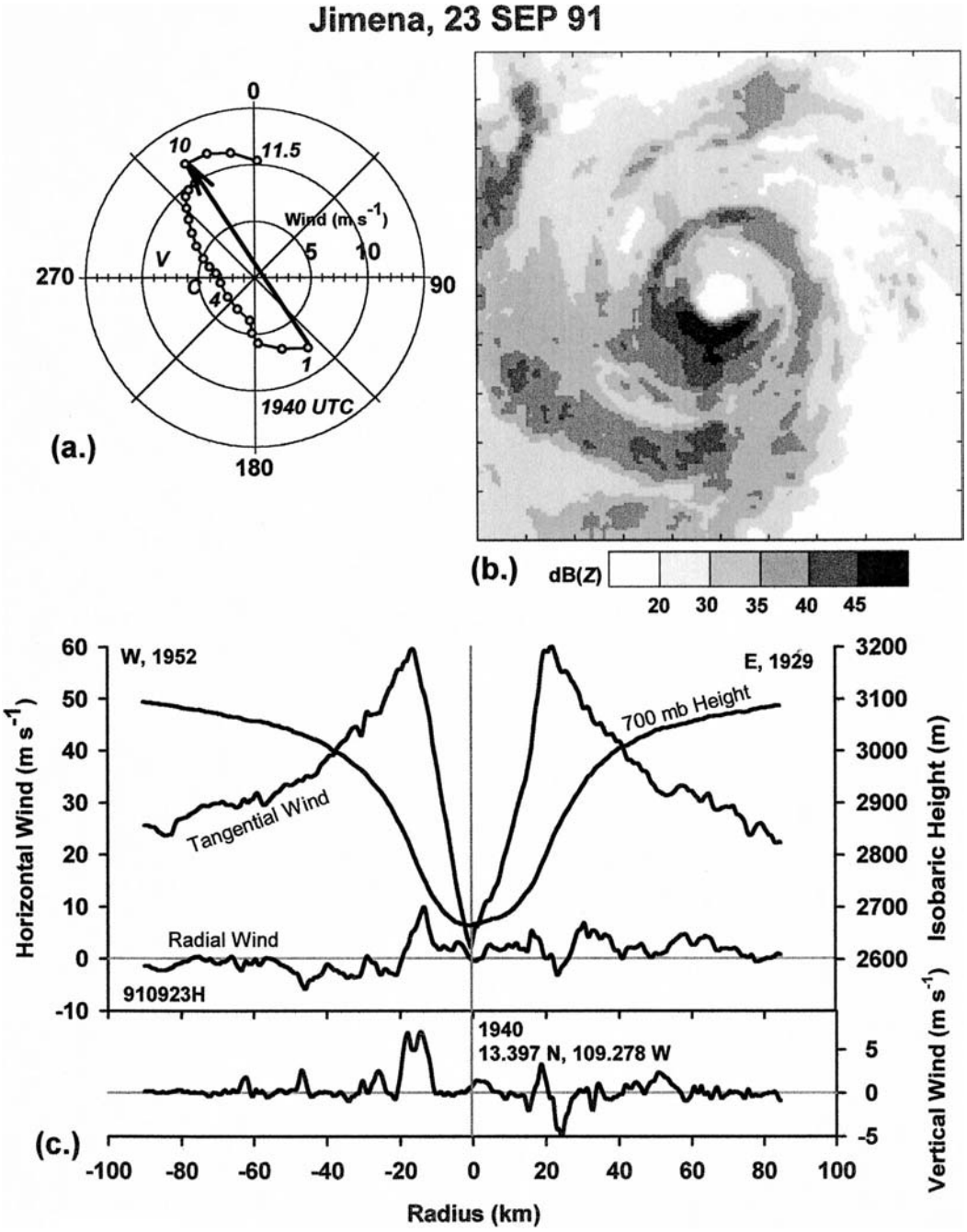

FIG. 5. Hurricane Jimena on 23 Sep 1991: (a) Doppler-determined hodograph of the storm-relative wind at 1940 UTC determined from the airborne dual-Doppler wind synthesis. The arrow indicates the largest lower-tropospheric shear. Here, C and V represent the storm motion and the vertically averaged wind, both expressed in a reference frame fixed to the earth. (b) A 240 km × 240 km square composite of PPI radar reflectivity for 1931–1951 UTC. (c) A profile of flight-level observations by *N42RF* on an east-to-west pass across the center at 700 hPa, 1929–1952 UTC.

By the time the echoes advected into the right semicircle, where they approached the tropopause, the reflectivity had decreased by ~20 dB(Z) through freezing and fall out of hydrometeors.

An east–west profile of flight-level data (Fig. 5c), oriented 45° to the shear, supports this description. It was observed 1929–1952 UTC coincident with the reflectivity composite. Outside the eyewall, the radial flow at 3 km tended to be inward on the west side and outward on the east. This flow was an example of the cross-vortex flow described by Willoughby et al. (1984). On the downshear side of the vortex where the low-level

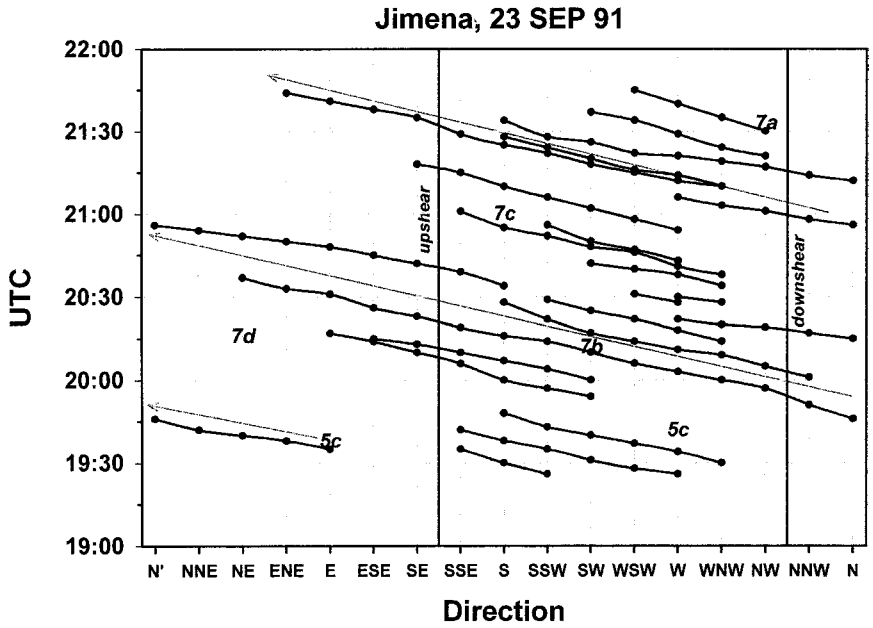

FIG. 6. Time–azimuth plots of individual radar echo positions in Jimena's eyewall based upon sweep-by-sweep animation of the aircraft PPI radar from 1926–2146 UTC on 23 Sep 1991. Time increases upward and echoes move from right to left, as they would appear to do from inside the eye. The shaded arrow marks the long-lasting cluster of cells, and figure numbers indicate locations of flight-level data and vertical-incidence radar cross sections from Figs. 5 and 7.

flow in the hodograph approached the eyewall, a 7 m s^{-1} updraft, nearly 10-km wide, appeared. It straddled the RMW near the upwind end of the high reflectivity semicircle. The radial flow at the updraft axis was outward at 10 m s^{-1}, consistent with an outward sloping updraft. On the eastern side, where the low-level, cross-vortex flow receded from the eyewall, a 4-km-wide 4 m s^{-1} updraft lay just inward from a 7-km-wide 5 m s^{-1} downdraft. The updrafts correlated with outflow, as one would expect in buoyant slantwise vertical motion that tends to follow inclined surfaces of constant angular momentum. This pattern of up- and downdrafts was typical during the flights in Jimena and Olivia. The aircraft generally encountered updrafts on the downshear side of the eye, and downdrafts, mixed with narrower, weaker updrafts diametrically across the eye on the upshear side. Since the time required for the aircraft to cross the eye and eyewall was ~5 min, the up- and downdrafts represent samples of different cells at different stages of their life cycles. The antisymmetric distribution of vertical motion across the vortex center implies that there was a strong azimuthal wavenumber-1 component of shear-induced vertical motion as well as of radar reflectivity. Similar asymmetries with similar relationships to the surrounding flow occur in numerical models (Bender 1997; Frank and Ritchie 1999, 2000) and were observed in Hurricanes Norbert of 1985 (Marks et al. 1992) and Gloria (Franklin et al. 1993). In agreement with the model results, echoes formed as the mean swirling flow entered the ascending cell of a shear-induced vertical-motion dipole. They grew through condensational heating in the left-of-shear semicircle, generating abundant hydrometeors, and their lower-tropospheric updrafts dissipated in the upshear descending cell.

Tracking of individual echoes in animated radar reflectivity fields of the eyewall provides a context for description of the reflectivity elements' life cycles and dynamics. These results appear in some detail because they bear on the hypothesis that spiral bands observed by radar are vortex Rossby waves (e.g., Chen and Yau 2001; Wang 2002). The echoes generally first appeared somewhat downstream of the downshear direction (Fig. 6). Initiation of the updrafts must have occurred upstream of this position because a few minutes are required for raindrops to grow large enough to have detectable radar reflectivity. Southwest of the center, where the composite reflectivity was high, cells often passed a given azimuth at intervals of 5–10 min. Most cells were trackable for ~135° from formation in the northwest through southwest quadrant to dissipation in the south through east quadrant. Lifetimes of the reflectivity features were typically 10–30 min.

There were, however, a few echoes that lasted ~1 h and could be tracked completely around the eyewall. These defined a cluster of features that circled the eye twice during the period of observation. The cluster was first marked as a single cell east of the center at 1935 UTC. Several short-lived cells appeared near it as it rotated past north into the downshear quadrant at 1945–2000 UTC. The original cell and most of the newly formed ones dissipated, but one new cell lived long

enough to rotate past north at 2055 UTC and again trigger a burst of convection in the downshear quadrant before it dissipated west of the center at 2105 UTC. Most of these newly formed cells again dissipated, but one survivor rotated to east-northeast of the center by 2145 UTC when the radar coverage suitable for animation ended. In the animated images, a sporadic wavenumber-2 pattern appeared during this time as rotating pairs of diametrically opposite cells modulated by the broad, stationary wavenumber-1 reflectivity asymmetry.

Examination of Fig. 6 shows that the long-lived cluster and the individual cells had slightly different rotation periods. The time from 1935 UTC, when the first cell of the cluster became trackable east of the center, through 2140 UTC, when the last trackable cell passed the same azimuth represents two complete revolutions, for an overall period of 62.5 min. Since each successive cell used to track the pattern formed upwind of its predecessor, a rotation period somewhat shorter than an hour is appropriate for the individual cells. For example, the first long-lived echo passed east of the center a second time after an interval of 55 min. By way of comparison, air at the RMW (19 km) moving with the wind there (57 m s^{-1}) had an orbital period of 35 min. Thus, these features propagated upwind so that the cluster of echoes moved at 56% of the wind speed at the RMW, and the individual echoes moved at 64%. The echoes' rotation at a speed slower than the free-atmosphere wind is consistent with earlier observations in Hurricane Frederic (Parrish et al. 1984) and with expectations for convectively excited vortex Rossby waves.

The convective structure is illustrated in greater detail by four time–height radial cross sections (Fig. 7) observed with vertical incidence Doppler radar. In the VI sections, the center of circulation is out of the frame to the left; the appearance of nonzero reflectivity about a quarter of the way across the panel represents the eye boundary; and the right side is ~25 km outside the eyewall. The structure was more complicated than the simple updraft–downshear, downdraft–upshear dipole suggested by the flight-level data and PPI composites. Convective motions tended to be collections of discrete bubbles rather than persistent, continuous drafts. Still, the data are consistent with updrafts that formed in the downshear semicircle of the eyewall. They reached maturity after moving ~90° around the eye, and developed precipitation-driven downdrafts in the upshear semicircle. As the updrafts moved past the upshear azimuth, they separated from the eyewall. They also generally detached from the boundary layer and joined the upper-tropospheric outflow. Condensate either precipitated or froze, resulting in lower radar reflectivity. The arc of low radar echos on the northeast side, opposite the mature updrafts, was thus filled with convective debris and downdrafts in the lower troposphere beneath glaciated, upper-tropospheric updrafts. The first VI cross section (Fig. 7a) captures a forming updraft. The second illustrates a deep vigorous updraft (Fig. 7b). The third shows a strong precipitation-driven downdraft (Fig. 7c), and the last depicts mixed up- and downdrafts in the lower reflectivities on the right side of the shear vector (Fig. 7d).

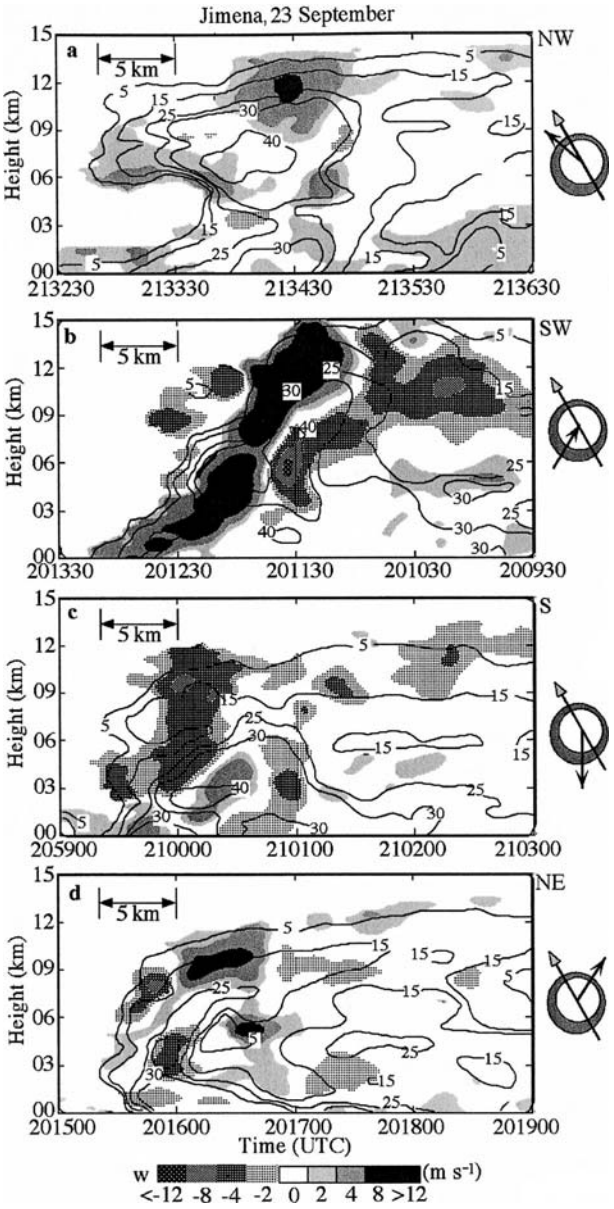

FIG. 7. Time–height cross sections of vertical velocity (shading) and radar reflectivity (contours) measured by the P-3's tail radars in Jimena on 23 Sep 1991. Schematics at the right indicate the shear (longer arrow) and flight track (shorter arrow) superimposed upon a representation of the eye. (a) Northwest of the center between 2132:30–2136:30 UTC; (b) southwest, 2009:30–2013:30, (c) south 2059:00–2103:00, and (d) northeast, 2015:00–2019:00.

In Fig. 7a, the detectable vertical velocities in an updraft along the inner edge of the eyewall northwest of the center were <5 m s^{-1} and confined below 6 km. This position was near or at the position where most trackable reflectivity features appeared. Between 1.5-

and 6-km altitude, a well-defined vault of low reflectivity (<5 dB*Z*) extended 7 km outward from the eye into the eyewall. The Doppler-determined vertical velocities were about 4 m s^{-1} at the top and bottom of the vault. *N42RF* measured a flight-level updraft >5 m s^{-1} as it flew through the scatterer-free volume at 4 km. This feature was the beginning of a convective updraft as it rose from the boundary layer. It was so new that its top had just reached the 0°C isotherm. Collision–coalescence had not had time to generate hydrometeors large enough to have substantial reflectivity or to fall against the updraft. A stronger, upper-level updraft, >8 m s^{-1}, appeared 12 km radially outward from the new updraft. Just below and inward from the second updraft was a region of reflectivity >40 dB*Z*, apparently due to hydrometeors falling from the updraft. Reflectivites in the draft itself decreased from almost 40 dB*Z* at the bottom to <5 dB*Z* at the top. The updraft was unloading most of its condensate as it approached the tropopause to join the upper-tropospheric outflow. This updraft seems to have been at a much later state of its life cycle, probably after it had completed an orbit around the eye.

Observations taken more than an hour earlier showed the strong updraft (Fig. 7b) of the first long-lived echo in Fig. 6. It had by that time rotated 225° around the storm to the center of the composite PPI reflectivity maximum on the left side of the shear vector, southwest of the center. The 5-km-wide updraft extended from near the surface to 15 km. It was just outward from the strong reflectivity gradient, and sloped radially outward with height along the edge of the eye. The vertical velocities were >4 m s^{-1} throughout most of the depth of the troposphere, but the fastest updrafts were >12 m s^{-1} in three discrete bubbles. The largest upward velocity was 17 m s^{-1} at 11-km altitude. A strong midlevel downdraft occurred radially outward and beneath the updraft. The strongest downward motion was 14 m s^{-1} at 5-km altitude, coincident with heavy precipitation enclosed inside the 40-dB*Z* contour straddling the melting level at 6-km altitude. A second plume of descending air, 10–15-km wide, appeared at 7–14-km altitude. Its peak downdraft was >12 m s^{-1}. It probably originated near the tropopause, as observed in the eyewalls of other hurricanes with strong updraft–downdraft couplets (Black et al. 1994). Smaller areas with 2–5 m s^{-1} downdrafts occurred at 9–12-km height inside the eye where the reflectivity was ~5 dB*Z*. They may have been air cascading down the inner edge of the eyewall after it detrained from the eyewall updraft (Willoughby 1998). The vertical profile of precipitation and vertical velocity in Fig. 7b resembled the conventional conceptual model of the axisymmetric eyewall (Jorgensen 1984b), although the vertical motions in Jimena were stronger than in the model.

A VI section south of the center, near the downwind end of the composite PPI reflectivity maximum (Fig. 7c) shows an entirely different radius–height profile. Radar reflectivity >30 dB*Z* was largely confined below 6-km altitude, and the profile was marked by strong precipitation-driven downdrafts. The largest downdraft was 5 km wide and extended from 12- to 3-km altitude along the inner edge of the eyewall. Peak values were >8 m s^{-1}, not as strong as the less extensive downdrafts in Fig. 7b. A small area of upward motion appeared near the surface at the boundary between the eye and eyewall. A 4 m s^{-1} updraft was radially outward from the main downdraft, and a 4 m s^{-1} downdraft lay beyond it. They extended upward to only about 5–6 km. A hump of reflectivity >30 dB*Z*, with a core of reflectivity >40 dB*Z*, spanned the boundary between the main downdraft and the second updraft. Reflectivity decreased rapidly with altitude in the upper troposphere. The 5-dB*Z* contour reached only to 11–12 km in Fig. 7c, compared with >15 km in Fig. 7b.

Between passages of the long-lived cells, the low-reflectivity northeastern semicircle of the eyewall contained mixed ascent and descent (Fig. 7d). The 5-dB*Z* contour was below 12 km altitude here as well. This cross section represented the late stage of the convective elements' life cycles. It contained a single >8 m s^{-1} updraft 5 km outward from the eye boundary with only 15–20-dB*Z* reflectivity at its center. A line of three other cells with 2–4 m s^{-1} rising motion appeared at 12–13 km along the 5-dB*Z* contour in the upper troposphere. A sloping tail of 1–2 m s^{-1} ascent extended from the main updraft downward, parallel with the eyewall boundary, to 3-km altitude. A band of reflectivities >25 dB*Z* paralleled the tail from the surface to a point below the main updraft at 8 km. On either side of the tail were bubbles of descent. The inner bubble had 6 m s^{-1} vertical velocity in the gradient of reflectivity at the eyewall boundary. It was apparently driven by evaporation as condensate-laden air in the eyewall mixed with dry air from the eye (Willoughby 1998). The second bubble, with a 4 m s^{-1} downdraft, was in 30-dB*Z* reflectivity beneath the updraft. The high reflectivity suggests that it was driven by precipitation loading. Similar reflectivities, >30 dB*Z*, lay below 2-km altitude under the updraft–downdraft complex. A second updraft, smaller and shallower than the main one, but nearly as strong, rose about 10 km outward from the eyewall. A broad area of stratiform rain extended outward from this cell.

On 24 September 1991, Jimena continued to move westward over SST ~ 28°C. Although extreme range from Puerto Vallarta and availability of only one aircraft resulted in less complete observations, a consistent picture of the storm's interaction with its surroundings emerged. The hurricane's motion slowed to 5 m s^{-1} as the maximum shear backed 115° to northeasterly and weakened to 13 m s^{-1} (Fig. 8a). In the layer of maximum shear, from 0.5 to 8.0 km, vertical changes in speed predominated. Above 8 km, the hodograph veered by 70° but maintained 4–6 m s^{-1} speed. In the PPI composite, the principal band was less extensive than on the previous day. It wrapped around the southeastern semicircle and joined the northwestern eyewall. Maximum

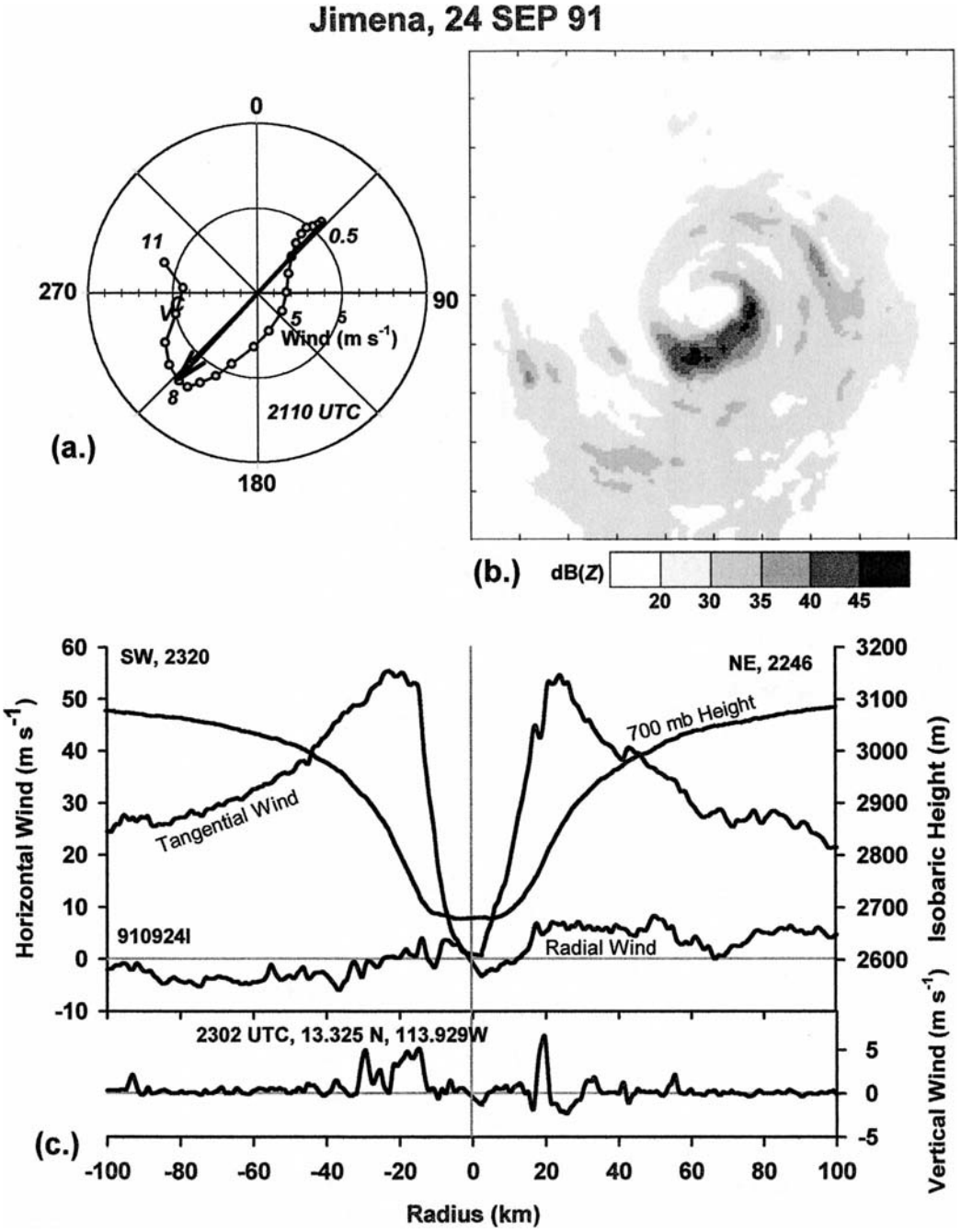

FIG. 8. Hurricane Jimena on 24 Sep 1991: (a) Doppler-determined relative-wind hodograph at 2110 UTC with shear, storm motion, and earth-relative vertically averaged wind indicated as in Fig. 5. (b) A 240 km × 240 km square PPI composite for 2255–2319 UTC. (c) A profile of flight-level observations by *N42RF* on a northeast-to-southwest pass across the center at 700 hPa, 2246–2320 UTC.

reflectivity shifted to the southeast semicircle to remain on the left side of the low-level shear vector (Fig. 8b). The eye had expanded to 22-km radius. Simultaneous flight-level observations (Fig. 8c) showed a broad updraft with two ~5 m s^{-1} peaks on the downshear, southwest side of the eyewall and a 5-km-wide 7 m s^{-1} updraft inward from a 10-km-wide 3 m s^{-1} downdraft on the upshear, northeast side. The updraft may have represented a ''tail'' extending downward from an updraft centered above flight level, as illustrated in Fig. 7d. On the downshear side of the vortex, 5 m s^{-1} inflow penetrated to the eyewall; on the upshear side somewhat stronger outflow receded from the eyewall. This pattern is consistent with storm-relative inflow from the south-

west and outflow toward the northeast shown in the hodograph. Vertical incidence sections of convective structure and cell tracking were not available on 24 September because the dual-beam antenna on *N43RF* did not sweep through zenith or nadir. The duration in the storm was too short to provide useful PPI animation.

4. Hurricane Olivia

On 24 September 1994 the WP-3Ds staged from Puerto Vallarta to observe Hurricane Olivia, >1400 km to the SW. After 1934 UTC when *N42RF* and *N43RF* reached their initial points, they flew at 3.0- and 4.2-km-pressure altitude. Throughout the flights on both days, the Doppler radars scanned normal to the flight tracks during radial penetrations, and used FAST on downwind legs. The aircraft completed seven coordinated traverses in 4 h as the storm moved northwestward at 7 m s^{-1}, and deepened at a rate of 2 hPa h^{-1}. During the night after the first flights, Hurricane Olivia continued to intensify and turned more toward the north. At 2033 UTC, *N42RF* and *N43RF* entered Olivia and flew a total of eight coordinated passes, although the last one departed significantly from the plan. Olivia's motion during the second mission was slower, toward the north-northeast at 4 m s^{-1}.

Olivia's initial structure and intensity were strikingly similar to Jimena's, but Olivia, in contrast with Jimena, intensified. Linear trends fitted to both days' data at 600 hPa together show that between 2200 UTC on 24 September and 2200 on 25 September, the maximum flight-level wind increased from 57 m s^{-1} to 60 m s^{-1}; the RMW decreased from 16 to 13 km; and height of the 600-hPa surface fell from 3980 to 3840 m. But the 2 days considered together tell only part of the story because the changes during each day were so different. When the days were treated individually (Fig. 9), 24 September clearly showed intensification and 25 September clear weakening. On 24 September, the maximum flight-level wind increased from 55 to 59 m s^{-1} as the RMW contracted from 17 to 15 km. On 25 September the wind decreased from 64 to 54 m s^{-1} as the RMW expanded from 11 to 16 km. On 24 September the 600-hPa height fell nearly 50 m; on 25 September it rose >100 m.

The data have so much scatter that only 600-hPa height shows an unambiguous trend above the scatter. The convective-ring model (Shapiro and Willoughby 1982) predicts strengthening maximum wind and contracting RMW when the 600-hPa height falls and weakening maximum wind and expanding RMW when it rises. Figure 9 exhibits the former correlation on 24 September and the latter on 25 September. Independent observations by the other aircraft at 700 hPa show the same pattern, except for the wind on 24 September, which appeared to decrease. Under the null hypothesis that the scatter is so large that the slope of the temporal trend may have either sign, the number of agreements

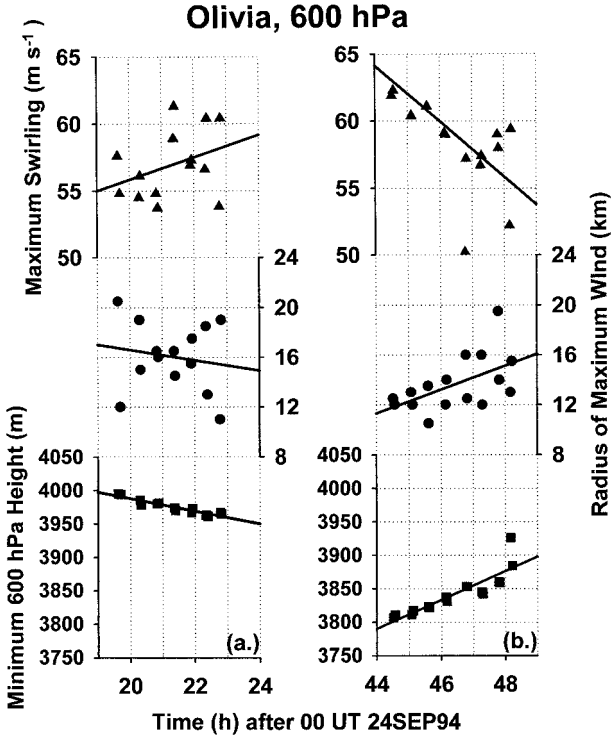

FIG. 9. Obs max wind, radius of max wind, and height of the 600-hPa surface obs in Hurricane Olivia on 24 and 25 Sep 1994 with each day treated individually. Lines are least squares fits to the observations for the times when the aircraft was in the storm.

in sign between the fitted slopes and the a priori expectation from the convective-ring model obeys a binomial distribution with $p = 0.5$. The cumulative probability of complete agreement or only one disagreement is 3.5% in this distribution. Thus, it is extremely unlikely that the pattern of intensity change arose by chance from random scatter in the observations.

Thus, Olivia intensified over 28°C water that could support MPI of 925 hPa, essentially the same as the actual lowest sea level pressure attained. On the next day, Olivia weakened over 27°C water that cooled to 26.5°C during the course of the flight (Fig. 2). The corresponding MPI was 943–950 hPa. Upward mixing of cold water in the climatologically shallow preexistent mixed layer just south of the strong SST gradient may have combined with Olivia's slower motion to reduce SST under the storm further. Another possible reason for weakening is intrusion of dry, somewhat cooler air from the north. It is possible that Olivia's small eye at the start of the weakening rendered it somewhat more vulnerable to shear than Jimena was. On the other hand, the wind at the ends of the flight-level profiles were essentially the same in both storms, so that it is difficult to argue that Olivia's vortex as a whole was more compact.

On 24 September, the greatest environmental shear in the hodograph was 8 m s^{-1} (Fig. 10a) from the east-

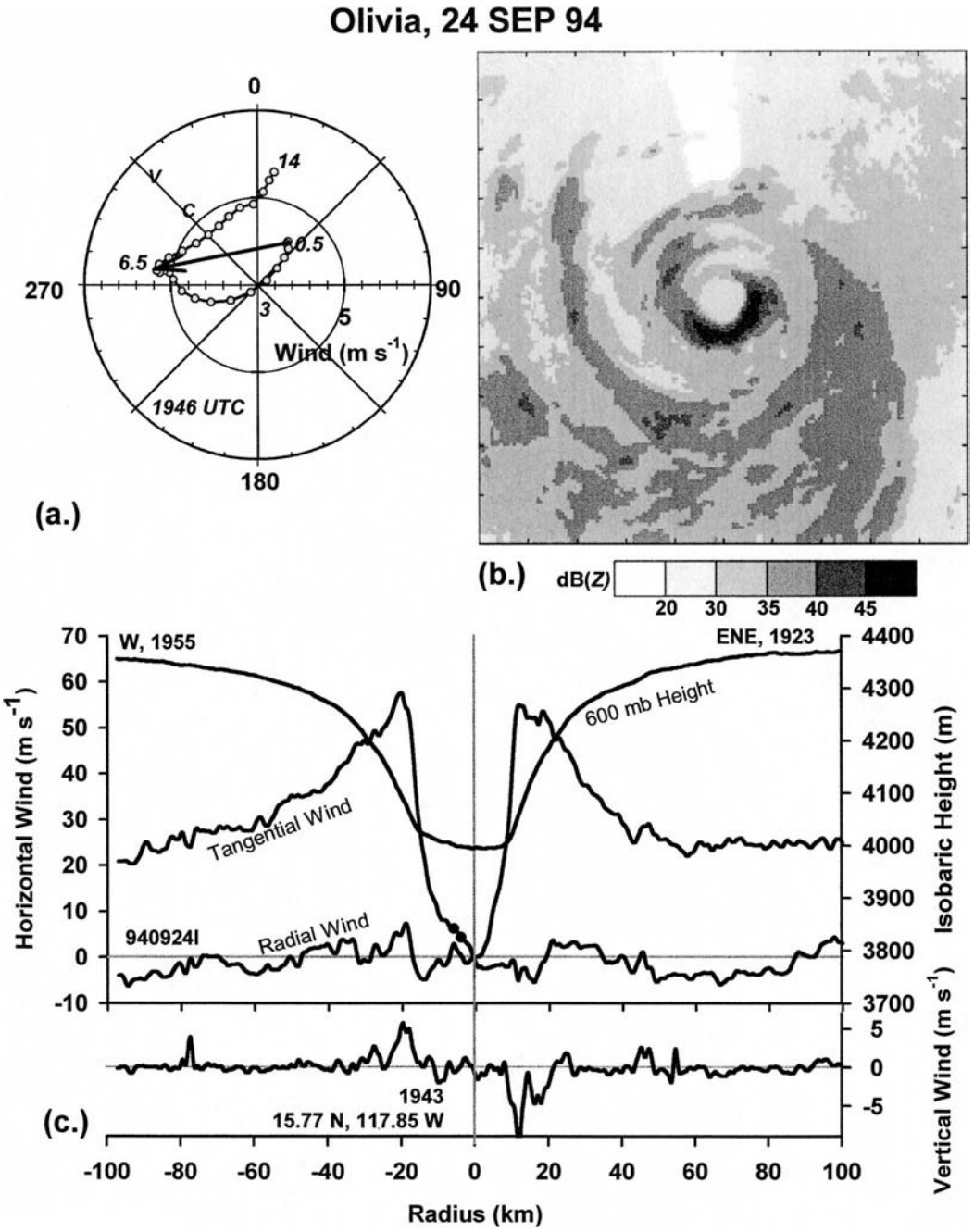

FIG. 10. Hurricane Olivia on 24 Sep 1994: (a) Doppler-determined relative-wind hodograph, storm motion, and earth-relative vertically averaged wind at 1946 UTC. (b) A 240 km × 240 km PPI composite for 1934–1956 UTC. (c) A profile of flight-level observations by *N42RF* on an east-northeast-to-west pass across the center at 600 hPa, 1923–1955 UTC.

northeast between 0.5- and 6.5-km altitude. It was about half as strong as in Jimena. The vertically averaged wind in the hodograph was also 8 m s^{-1} from the southeast, compared with a motion of 6.5 m s^{-1} toward the northwest. At low levels, the flow relative to the hurricane was from the southwest at 3 m s^{-1}, decreasing to zero by 3 km. Above that altitude, it increased to 6 m s^{-1} and veered to blow from the east. It kept about the same speed above 7 km, but continued to veer to blow from the south-southwest by 14 km.

The composite PPI radar structure (Fig. 10b) was similar to Jimena's and to Frank and Ritchie's (2000) simulation in 5 m s^{-1} easterly shear. A secondary band partially encircled the eye from the west side. It was

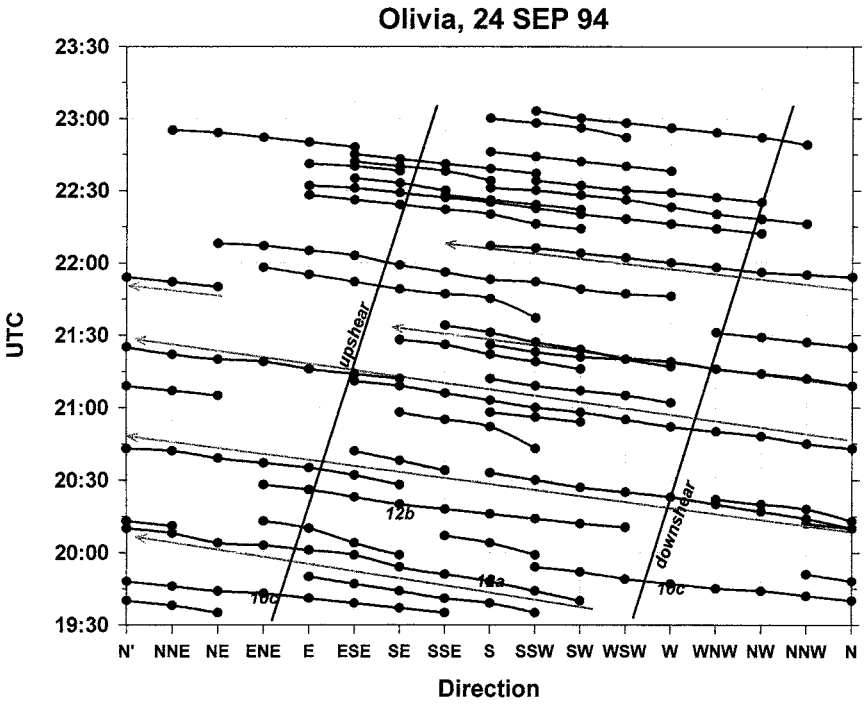

FIG. 11. Time–azimuth plots of individual convective cells in Olivia's eyewall from 1935–2304 UTC on 24 Sep 1994. Figure numbers indicate locations of flight-level data and vertical-incidence radar cross sections in Figs. 10 and 12.

open to the northwest and joined the broad principal band, which spread east and south to southwest of the center. The principal band wrapped around the north side and connected with the western eyewall. Highest reflectivities in the eyewall were concentrated in the southern semicircle, to the left of the low-level shear vector. Discrete radar echoes formed on the west side of the eyewall. They reached maximum reflectivity >45 dB*Z* south and east of the center. Reflectivity decreased after they advected around the storm to the right side of the low-level shear vector. In the northern semicircle reflectivities were generally ~30 dBZ. At 600 hPa, a west-to-east-northeast profile of flight-level observations (Fig. 10c), nearly along the low-level shear vector, showed 58 m s^{-1} maximum winds at 21-km radius on the west side of the eye and 55 m s^{-1} maximum winds at 12.5 km on the east. The outer vortex was comparable in strength with Jimena's with winds of 20–25 m s^{-1} at the ends of the profiles, 100 km from the center. Unlike Jimena, however, radial flow at 4-km altitude in the weaker shear was generally symmetric: on both sides of the eye it was outward within 40–50 km of the center and inward out to 80 km. Beyond the bands at 80–90 km, the radial flow was consistent with the relative flow below flight level in the hodograph—inward on the west and outward on the east-northeast side. This pattern suggested that the principal band acted as a partial barrier (Willoughby et al. 1984) that protected the vortex core from an environmental relative flow that was somewhat stronger and deeper than that represented in the hodograph. A 5.7 m s^{-1} updraft appeared on the west side of the eye and a 10.5 m s^{-1} downdraft on the east. The 600-hPa height profile inside the eye was flat. The minimum height was displaced nearly 7 km from the geometric center of the eye and the axis of vortex rotation, to a position adjacent to the greatest reflectivity, in the eastern downdraft.

Time–azimuth tracking of cells in Olivia's eyewall (Fig. 11) yielded results similar to those in Jimena. Early in the period, short-lived cells formed southwest of the center where the low-level flow approached the eye. Later in the period, as the Doppler-determined shear veered toward the northwest and strengthened to 15 m s^{-1} (not illustrated), the site of formation for most cells shifted to west-northwest of the center. Lifetimes of short-lived cells were comparable with those in Jimena, 10–20 min, long enough to advect 90°–180° around the eye. There was also a cluster of long-lived cells that could be clearly tracked for three orbits between 1940 and 2140 UTC and may have persisted for another whole orbit subsequently. The orbital periods of the long-lived cells were 40–45 min. Three orbits of the cluster between 1940 and 2140 UTC is equivalent to a period of 40 min. Air moving with the mean swirling wind (57 m s^{-1}) at the RMW (16 km) would circle the eye in 29 min. Thus, the orbital velocity of the cluster was about 72% of the wind's. Between 2215 and 2345 UTC, convection blew up on the south side of the eye. During this outburst, and also during a similar, less pronounced one between 2050 and 2135 UTC, cells passed

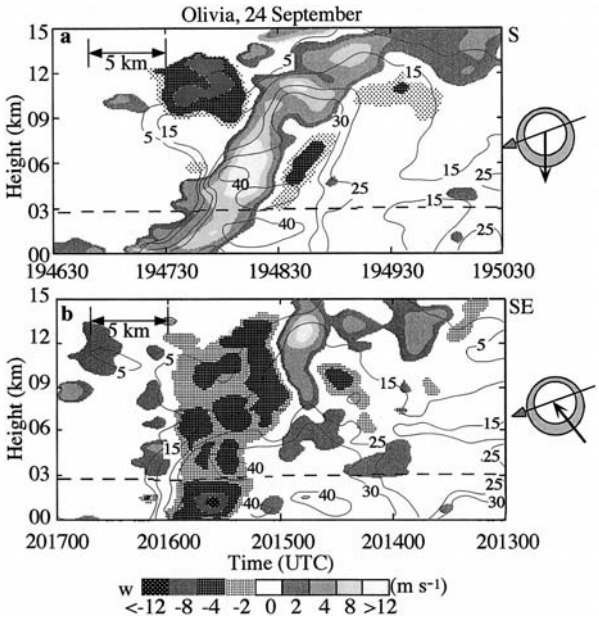

FIG. 12. Time–height cross sections of vertical velocity (shading) and radar reflectivity (contours) measured by the P-3's tail radars in Olivia on 24 Sep 1994: (a) south of the center at 1946:30–1950:30 UTC, and (b) southeast, 2013:00–2017:00.

a given azimuth in the left-of-shear quadrant at 5-min intervals. At other times and outside the region of high composite reflectivity the time between successive cells was 10–15 min, or longer.

Vertical incidence sections observed 75 and 45 min before Fig. 10c illustrated the structure of the convective cells' updrafts and downdrafts in the southern eyewall. The animated reflectivity fields show that from 1944 through 1957 UTC, the southern eyewall was filled with an arc of reflectivity >46 dB*Z* in which it was difficult to track individual cells. As the aircraft passed through the arc on a north-to-south exit of the eye, it encountered a deep updraft that contained three separate bubbles, each exhibiting peak speeds >12 m s^{-1} (Fig. 12a). The strongest was centered near 6 km. Vertical velocity was organized into an envelope of ascent >4 m s^{-1} that extended from the sea surface to 15 km, and sloped outward along the inner edge of the southern eyewall. It appeared to spread outward along the tropopause. The 5-dB*Z* reflectivity contour extended above 15-km altitude. Along much of the updraft the vertical wind speed was >8 m s^{-1}, just stronger than the terminal velocity of most hydrometeors (Gunn and Kinser 1949). This feature was a mature updraft, 80° to the left of the shear vector. Its structure was much like that observed in Jimena (Fig. 7b) at a similar location relative to the shear and reflectivity field. A wide volume of radar reflectivity >30 dB*Z* with local maxima >40 dB*Z* extended below and outward from the updraft axis. A narrower, 4 m s^{-1}, downdraft paralleled the updraft between 3- and 8-km altitude in the 30–40-dB*Z* reflectivity. The high reflectivity is consistent with the downdraft's being driven by condensate loading and evaporative cooling as hydrometeors fell out of the sloping updraft. A shelf cloud with 15-dB*Z* reflectivity protruded >5 km from the eyewall into the eye at 6–10 km. It was observed visually as well as by radar. The low reflectivity does not necessarily imply low condensate concentration inasmuch as hydrometeors were almost certainly frozen at that altitude. A strong (8 m s^{-1}) downdraft above the shelf cloud suggests a vertical velocity couplet—the Doppler radar signature of rotation around a nearly horizontal axis along the inner edge of the eyewall. At 12-km altitude, horizontal flow from the eyewall apparently advected snow and graupel into the eye, turned downward and rejoined the eyewall, leaving the hydrometeors to fall as virga inside the eye.

Another section across the eyewall in a different echo 30 min later and 20 km downwind, in the highest reflectivity of the southeast semicircle (Fig. 12b) was dominated by descent. This feature appears to have been at a later stage of its life cycle. It resembled a downdraft observed in Jimena (Fig. 7c) at a similar location relative to the shear and reflectivity patterns. A 5-km-wide downdraft containing multiple small-scale bubbles extended from the upper troposphere to the surface, where the most rapid descent, >12 m s^{-1}, occurred in 40-dB*Z* reflectivity. Smaller, discontinuous bubbles of ascent flanked the downdraft. In contrast with the sloping updraft in Fig. 12a, the downdraft was essentially vertical. An overhang of low (5 dB*Z*) radar reflectivity protruded from the eyewall into the eye near 11-km height. Just outward from the main downdraft was a narrow updraft with 12 m s^{-1} maximum ascent at 13 km, connected to two weaker cells farther out. These features appear to have been the remains of the updraft that caused the downdraft. One plausible explanation for downdrafts in the eyewall invokes condensate loading and cooling by evaporation or melting of hydrometeors (Srivastava 1987; Marks and Houze 1987; Black et al. 1994). Generally vertical orientation of the downdrafts, parallel with the trajectories of falling condensate and coincident with high reflectivity, support this interpretation. On the other hand, their strength and upper-tropospheric origin suggest that they may have been dynamically induced, perhaps through moist symmetric instability, as described by Black et al. (1994) in Hurricane Emily of 1987.

As shown in Fig. 9, Olivia intensified overnight between flights while the environmental shear weakened ahead of a midtropospheric trough. The end of the intensification apparently coincided with Olivia's reaching SST < 27°C that continued to decrease during the course of the flight, so that the actual central surface pressure was 20 hPa below the MPI. An hour after the airplanes arrived on 25 September, the shear had increased from <3 m s^{-1} to ~4 m s^{-1} from the west (Fig. 13a). The PPI reflectivity field was more symmetric (Fig. 13b). Olivia's eyewall was surrounded by reflectivity >30 dB*Z* reflectivity, with values of 40–45 dB*Z*

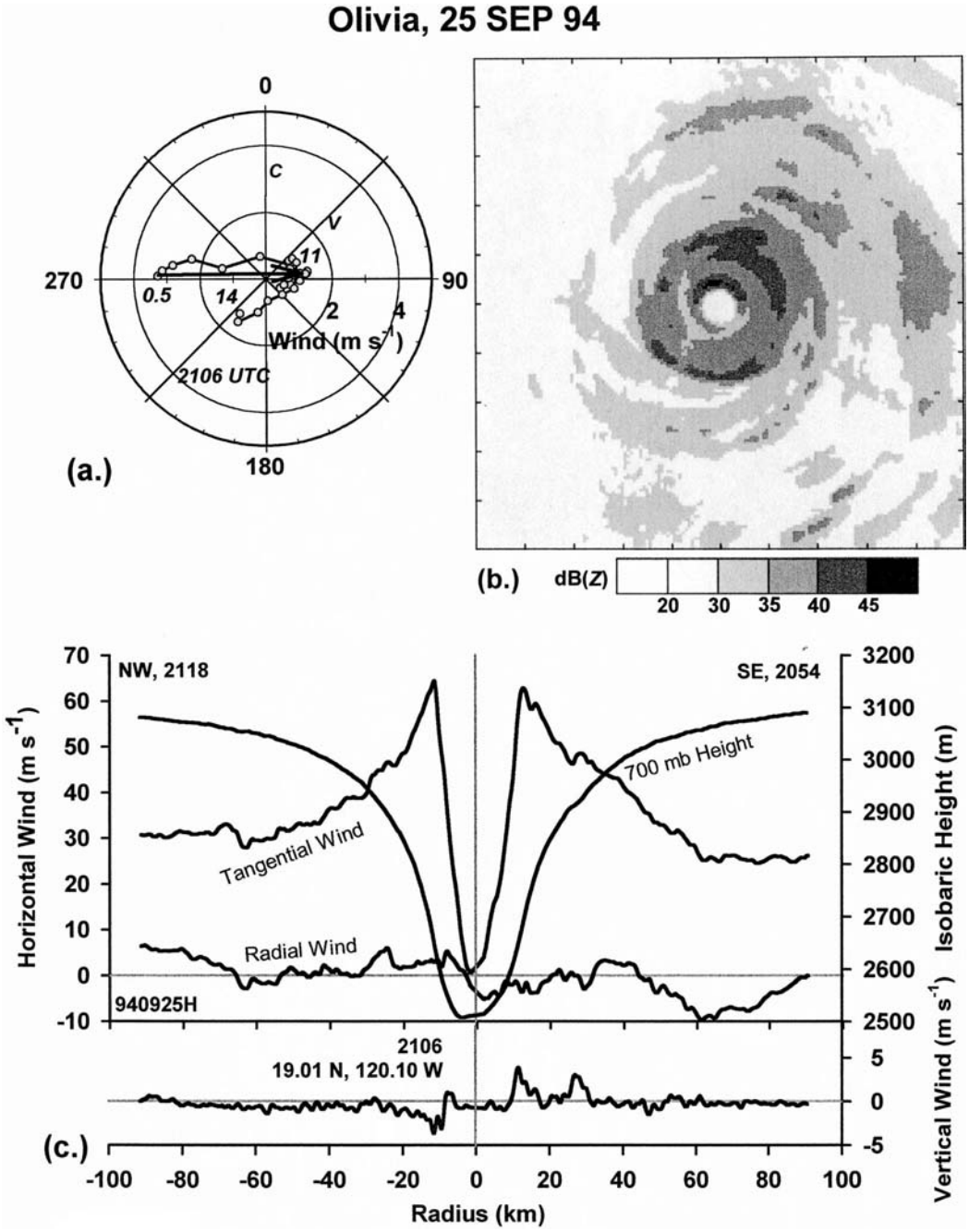

FIG. 13. Hurricane Olivia early in the day on 25 Sep 1994: (a) Doppler-determined relative-wind hodograph, storm motion, and earth-relative vertically averaged wind at 2106 UTC. (b) A 240 km × 240 km square PPI composite for 2054–2117 UTC. (c) A profile of flight-level observations by *N42RF* on a southeast-to-northwest pass across the center at 700 hPa, 2054–2118 UTC.

in the northern semicircle. Two outer rings of elevated reflectivity, at 25 and 60 km from the center, had formed around the inner eyewall as the shear decreased. These events suggested that Olivia was in the early stages of an eyewall replacement (Willoughby et al. 1982). The outer ring was at more or less the same radius as the secondary band on the previous day. A northwest-to-southeast profile of flight-level winds (Fig. 13c) is representative of data that showed subtle, sporadic maxima of horizontal wind at 25 and 60 km associated with the reflectivity rings. Maximum winds in the eyewall were 63–64 m s^{-1} at 12-km radius. The smaller eye notwithstanding, the rest of the wind profile was as broad as on the previous day or in Jimena, with 25–30 m s^{-1}

winds at 90–100-km radius. As in Fig. 10c, the 700-hPa height minimum was displaced 4 km from the central stagnation point toward the downdraft. This displacement is probably a convectively induced transient. The radial flow beyond 60 km was outward on the northwest side and inward on the southeast. This pattern suggests that the outer ring protected the vortex core from westerly relative flow as the principal band had on 24 September. Thus, the hodograph in Fig. 13a, which was based upon observations between 20- and 30-km radius, may underestimate the actual relative flow outside the vortex at flight level. High radar reflectivity in the eyewall notwithstanding, vertical velocities early on 25 September were much weaker than previously. On the southeastern (downshear) side of the eyewall, the airplane flew through a 3.9 m s^{-1} updraft in the eyewall and a 3 m s^{-1} updraft in the convective ring at 25-km radius; on the northeastern (upshear) side it encountered a 3 m s^{-1} downdraft in the eyewall. Vertical incidence sections (not shown) also supported a weakly asymmetric pattern of convection modulated to some extent by the smaller shear around the eyewall.

During the course of the flight, westerly shear across the vortex increased and eventually became >15 m s^{-1} from the west-northwest (Fig. 14a). As the shear increased, the storm filled much more rapidly than Jimena did in shear of comparable magnitude—perhaps because westerly shear appears to be more destructive than easterly shear (Tuleya and Kurihara 1981), but more probably because Olivia approached SST < 26.5°C and began to ingest dry air from the north simultaneously with the increase in shear. Although Olivia's eye on 25 September was smaller than Jimena's, its outer wind profile was similar, so that Olivia's more compact structure was probably not the reason for the greater vulnerability to shear.

In the PPI composites, the eyewall reflectivity became increasingly asymmetric as the shear strengthened. The high reflectivity region was still to the left of the shear, now on the northern side of the eyewall, opposite from where it was on 24 September (Fig. 14b). The outer rings of high reflectivity largely disappeared, so that convection in the northern eyewall was the dominant feature of the storm on PPI radar. Increasing shear and inflow of dry air from the cooler water to the north were probably responsible for the change. A similar transformation occurred in Atlantic Hurricane Gert of 1981 when it moved over cool SSTs and encountered westerly shear (Willoughby et al. 1984). As Olivia's outer convection weakened, the outer wind maxima shown in Fig. 13c disappeared. By 2300 UTC, vigorous convective cells in the northern eyewall grew to large horizontal extent and exhibited reflectivities >45 dB*Z*. At flight level, an 8 m s^{-1} updraft occupied the downshear (eastern) side of the eyewall and a 5 m s^{-1} downdraft occupied the upshear (western) side (Fig. 14c). As the relative flow due to stronger shear penetrated into the core, the earlier pattern of asymmetric radial flow became more pronounced. At 3 km the radial inflow predominated on the downshear side and outflow on the upshear side, as the storm moved eastward relative to the surrounding low-level air.

Before 2100 UTC when the environmental shear was low, the eyewall contained many persistent radar echoes that rotated completely around the eye (Fig. 15). A succession of echoes passed a given azimuth every 5 min, or even more frequently. Their orbital period was 22–25 min, compared with 19.5 min for air moving with the wind (64 m s^{-1}) at the RMW (12 km). Thus, the angular velocity of the cells was 80%–90% of the wind's.

As the environmental shear increased after 2100 UTC, high reflectivity became increasingly confined to the northern part of the eyewall, and lifetimes of the echoes decreased even as greatest reflectivities increased to >45 dB*Z* in the PPI composites. No coherent rotating group of cells could be identified after 2050 UTC. The echoes typically lasted 5–10 min and were confined to the left-of-shear *octant* of the eyewall. Vertically pointing Doppler radar observations show the vertical velocity structure of these short-lived features. One VI section (Fig. 16a) captured a developing updraft in a cell that could be traced for 45° from its initial appearance on the east side of the eye. In this instance, a >10 km-wide area of ascent with average 4 m s^{-1} velocity filled the eyewall below 4 km. Within the updraft were two bubbles with vertical velocity >8 m s^{-1}. The smaller bubble extended upward from the broad updraft. It was capped by >40 dB*Z* reflectivity and flanked by 2–4 m s^{-1} downdrafts. The cap is a consequence of the cell's ascent into a preexistent reflectivity field. In the low-reflectivity vault, minimum reflectivities were <5 dB*Z* because large drops had not yet grown through collision–coalescence.

A VI section between cells in the high-reflectivity region north of the center (Fig. 16b) shows reflectivites >40 dB*Z* confined below 4-km altitude. A broad, 8 m s^{-1} downdraft lay in a strong vertical gradient of reflectivities above the 40-dB*Z* layer. It appears to have been a precipitation-induced downdraft forced by hydrometeor loading and evaporation. The three narrow, 4 m s^{-1} updrafts along the eye boundary may have been the start of the echo that appeared north of the center at ~2250 UTC. Thus increasing shear and decreasing available thermodynamic forcing made the convective elements less organized, shallower, and shorter lived, despite higher radar reflectivities.

The entire dataset illustrates how variable the structure and evolution of these features were. Since the aircraft often encountered updrafts on the downshear side of the vortex, these cells must have generally formed 30°–45° of azimuth upstream of the downshear direction in order to have time to reach flight level and accelerate to the observed speed. Similarly, the aircraft sometimes encountered downdrafts, mixed up- and downdrafts, or even predominantly updrafts on the up-

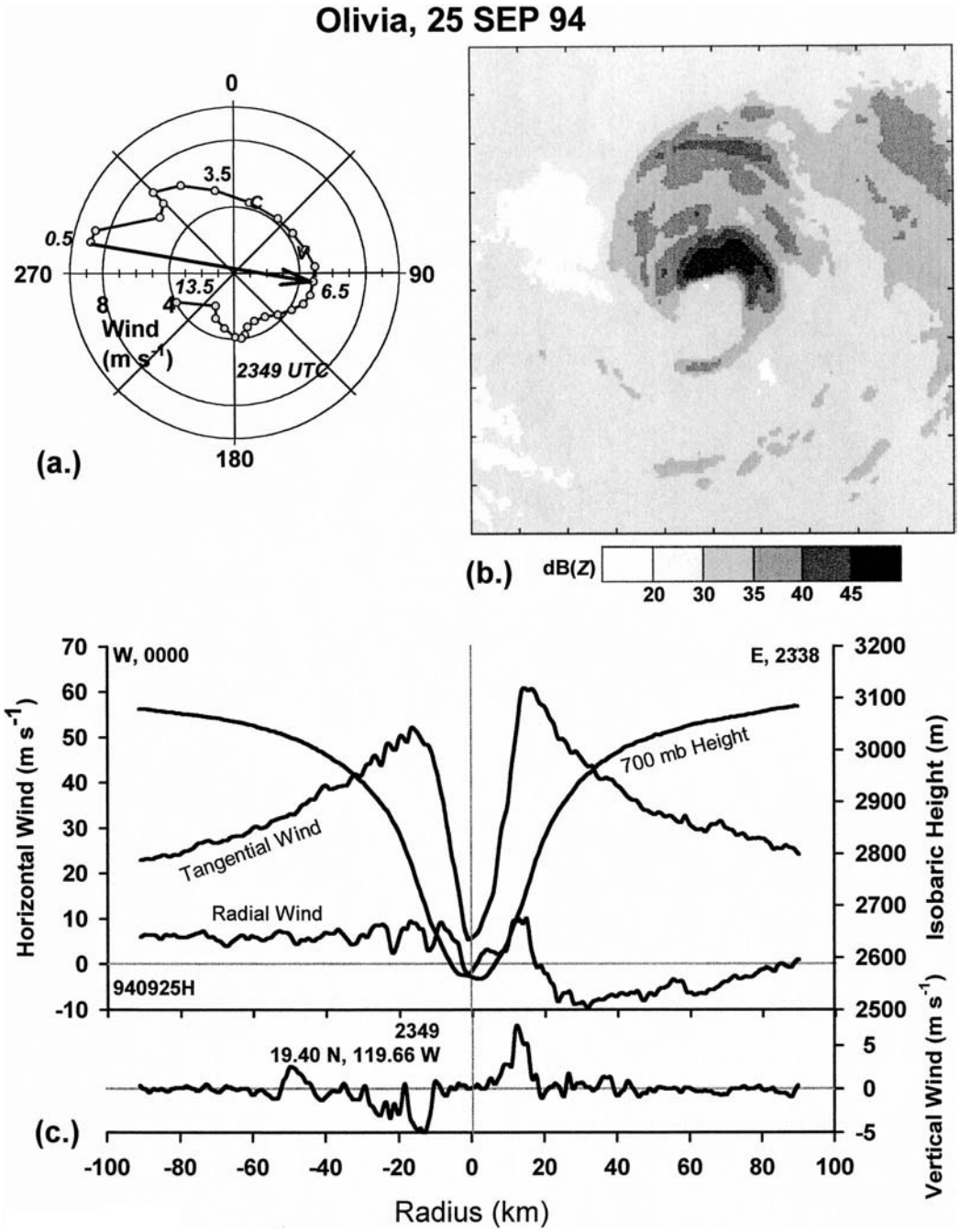

FIG. 14. Hurricane Olivia late in the day on 25 Sep 1994: (a) Doppler-determined relative-wind hodograph, storm motion, and earth-relative vertically averaged wind at 2349 UTC. (b) A 240 km × 240 km square PPI composite for 2338–2359 UTC. (c) A profile of flight-level observations by *N42RF* on an east-to-west pass across the center at 700 hPa, 2338–0000 UTC.

shear side of the center, nearly 180° around the eye from the locus of formation for most updrafts. Occasionally strong updrafts appeared at flight level in the generally low radar reflectivities to the right of the shear. Although these observations show that the echoes' origins and life cycles were variable, they also support a typical picture of growing updrafts in the generally downshear direction, increasing reflectivity as the cells advected around the storm and passed through the freezing level, and then decreasing reflectivity as condensate froze or fell out and the cells moved horizontally away from the eyewall in the upper troposphere.

Axisymmetric convective heating is known to spin up the vortex through the convective-ring mechanism

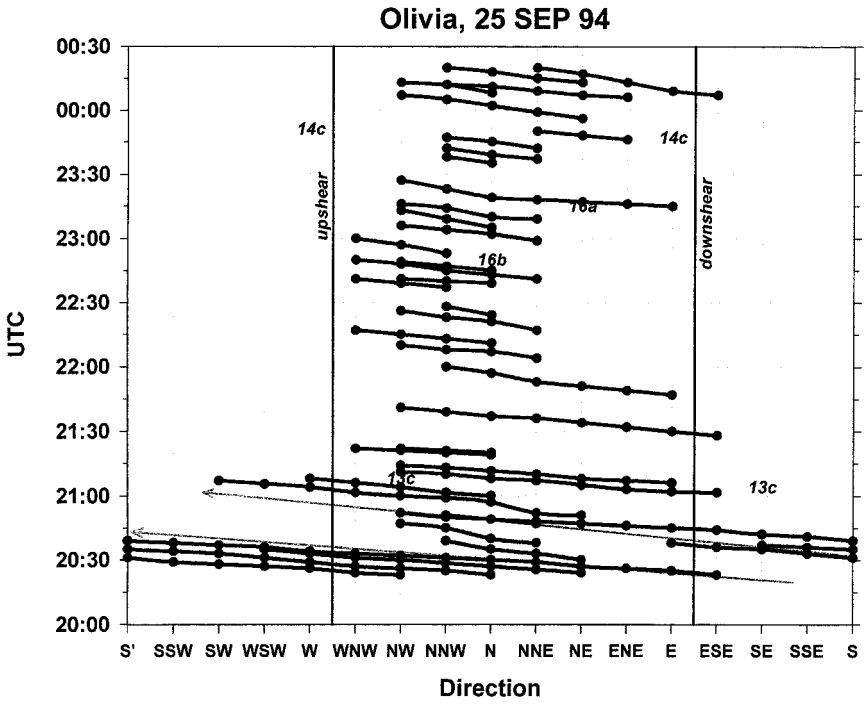

FIG. 15. Time–azimuth plots of individual convective cells in Olivia's eyewall from 2023–0024 UTC on 25 and 26 Sep 1994. Figure numbers indicate locations of flight-level data and vertical-incidence radar cross sections in Figs. 13, 14, and 16.

(e.g., Willoughby 1990). Plausible mechanisms have also been proposed for asymmetric convection to modify the axisymmetric structure of tropical cyclones (Montgomery and Kallenbach 1997; Montgomery and Enagonio 1998) through convectively excited vortex Rossby waves that sustain eddy momentum fluxes. While these mechanisms appear to have operated early on 25 September when Olivia was in weak shear, asymmetric convection modulated by environmental shear seems to have been unable to intensify the vortex as a whole later when the shear was stronger. The energy released appears to have been dissipated as gravity waves or other asymmetric motions. Asymmetric convection in Olivia and Jimena did not appear to excite track meanders correlated with convection as previous observational (e.g., Willoughby 1990) and theoretical studies (Willoughby 1992) suggest. Further theoretical study of the interactions between asymmetric heating and the mean vortex in the context of a continuously stratified, realistically scaled system are essential to understanding the motion and intensity change of convective, high-Rossby-number vortices in environmental shear.

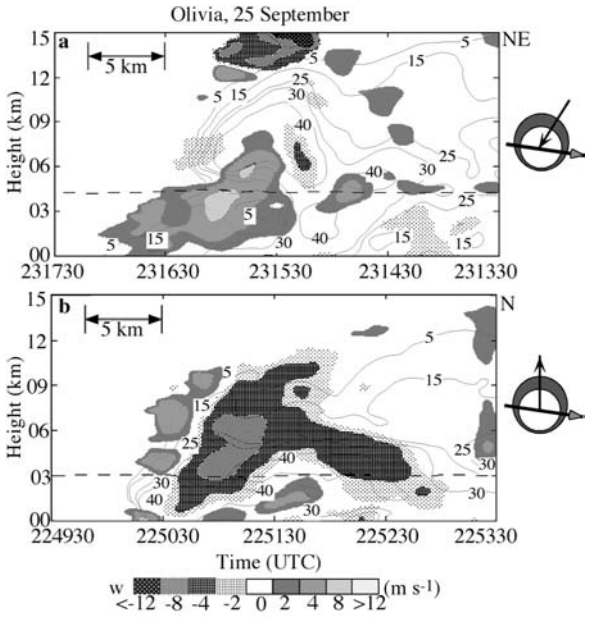

FIG. 16. Time–height cross sections of vertical velocity (shading) and radar reflectivity (contours): (a) Northeast of the center at 2313:30–2317:30; and (b) North at 2249:30–2253:30 on 25 Sep 1994.

5. Synthesis

Throughout the time it was observed, Jimena had asymmetrically distributed eyewall convection. It maintained constant intensity, or at most weakened slowly, in easterly shear over SST > 28°C. When the shear was <8 m s^{-1}, Olivia was able to intensify despite a similarly asymmetric distribution of convection. When the shear decreased to <5 m s^{-1} still over 28°C water, Oli-

via's convection became symmetrically distributed. Individual cells could then be tracked as they advected completely around the eyewall. Only when Olivia reached SST < 27°C and the shear reaching the vortex core increased to 14 m s^{-1} did it weaken rapidly. Flight-level data show that over warm SST outer bands with vigorous convection acted as barriers to the surrounding wind. Consequently, the shear in hodographs of Doppler-determined winds from just outside the eyewall tended to underestimate the true environmental relative flow. Jimena's ability to maintain category 4 intensity in 13–20 m s^{-1} shear and Olivia's significant strengthening in 8 m s^{-1} shear, support the hypothesis that a strong oceanic energy source reduces major hurricanes' vulnerability to shear. The bands' role in intensification, or at least in maintenance of intensity, is antithetical to the concentric eyewall phenomenon in which an outer band becomes a second eyewall that contracts around the original eyewall and supplants it, causing the storm to weaken (Willoughby et al. 1982). A consistent explanation of the change in Olivia's structure between Figs. 13 and 14 is that the diminished oceanic energy source weakened the convection in the bands outside the eye. The bands were neither able to become outer eyewalls nor to continue to act as barriers to environmental shear flow. Thus, drier air carried by the relative flow due to the shear was able to penetrate to the eyewall and contribute to the storms' weakening.

In both hurricanes, shear stronger than 8 m s^{-1} produced the wavenumber-1 distribution of convection shown schematically in Fig. 17. In composites of PPI radar data, the semicircle of the eyewall to the left of the shear vector contained the strongest reflectivities, often >45 dBZ. Model studies (e.g., Frank and Ritchie 2001) show that differential advection of the axisymmetric vorticity by the shearing storm-relative flow induces a vertical motion dipole with ascent on the downshear side and descent on the upshear side. Convection in Jimena and Olivia was periodic. Radar echoes formed near the downshear side of the eyewall and moved more slowly than the swirling wind, consistent with the properties of convectively excited vortex Rossby waves. They grew as they moved around the eye and reached maturity where the greatest composite reflectivity occurred on the left side of the shear vector. As they rose through the 0°C isotherm and rotated toward the upshear side of the eye, where the shear-induced descent was, the updrafts spawned precipitation-driven downdrafts in the lower troposphere. Thus, mixed up- and downdrafts predominated on the upshear side of the eyewall, generally with downdrafts in the lower troposphere overlain by updrafts in the upper troposphere. When the updrafts advected farther around the eye and migrated outward, the condensate fell out of them, and the downdrafts tended to weaken. Low reflectivity on the right side of the shear resulted not from a lack of vertical motion, but because the hydrometeors had either frozen or precipitated from updrafts. The unloaded updrafts accelerated upward. They approached the tropopause and separated from the eyewall as they passed through the right-of-shear semicircle.

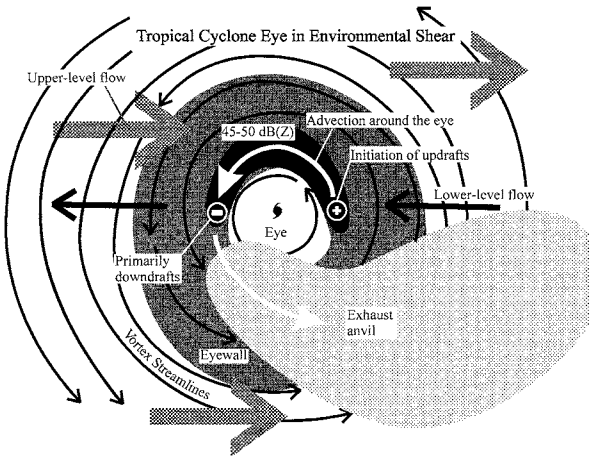

FIG. 17. Schematic illustration of the shear-induced convective asymmetry based upon observations of Jimena and Olivia. The low-level environmental flow is indicated by the two solid black arrows. Upper-level flow is indicated by the three stippled arrows. Convective cells form somewhat upwind of the downshear side of the eyewall. They advect around the eye into the semicircle to the left of the shear vector where warm rain processes generate hydrometeors large enough to reflect radar effectively. Precipitation-driven downdrafts begin about 90° to the left of the shear vector. By the time the cells reach the upshear side of the eyewall they have ascended through the 0°C isotherm and downdrafts predominate below 6 km. As the cells move into the semicircle on the right of the shear vector, most condensate freezes or falls out of the active updrafts. The unloaded updrafts accelerate upward. They detach from the eyewall and approach the tropopause as they rotate through the semicircle to the right of the shear.

In weaker shear, the shear-induced vertical motion dipole was also weaker. Clusters of convection, marked by a few long-lived echoes, could be tracked completely around the storm for multiple orbits. The clusters moved somewhat more slowly than the individual echoes because new echoes formed upwind of preexistent ones. Each time the clusters passed through the downshear to the left-of-shear quadrant, new short-lived convection triggered.

Acknowledgments. We thank Paul Reasor, Rob Rogers, and an anonymous reviewer for insightful comments on earlier drafts. Dean Churchill and Peter Black aided our understanding of the hurricanes' synoptic and oceanic environments. Jeff Hawkins provided the OTIS SST data. As always, we acknowledge our colleagues at NOAA's Aircraft Operations Center, without whose professionalism, dedication, and skill, studies such as this would be impossible. Finally, we are deeply grateful to Bob Burpee, former director of HRD, for his leadership and inspiration. Olivia was the last time he flew with us in a hurricane.

REFERENCES

Bender, M. A., 1997: The effect of relative flow on the asymmetric structure in the interior of hurricanes. *J. Atmos. Sci.,* **54,** 703–724.

Black, M. L., R. W. Burpee, and F. D. Marks Jr., 1996: Vertical motion characteristics of tropical cyclones determined with airborne Doppler radial velocities. *J. Atmos. Sci.,* **53,** 1887–1909.

Black, R. A., H. B. Bluestein, and M. L. Black, 1994: Unusually strong vertical motions in a Caribbean hurricane. *Mon. Wea. Rev.,* **122,** 2722–2739.

Bosart, L. F., C. S. Velden, W. E. Bracken, J. Molinari, and P. G. Black, 2000: Environmental influences on the rapid intensification of Hurricane Opal (1995) over the Gulf of Mexico. *Mon. Wea. Rev.,* **128,** 322–352.

Chen, Y., and M. K. Yau, 2001: Spiral bands in a simulated hurricane. Part I: Vortex Rossby wave verification. *J. Atmos. Sci.,* **58,** 2128–2145.

DeMaria, M., 1996: The effect of vertical shear on tropical cyclone intensity change. *J. Atmos. Sci.,* **53,** 2076–2087.

——, and J. Kaplan, 1994: Sea surface temperature and the maximum intensity of Atlantic tropical cyclones. *J. Climate,* **7,** 1324–1334.

——, J.-J. Baik, and J. Kaplan, 1993: Upper-level angular momentum fluxes and tropical cyclone intensity change. *J. Atmos. Sci.,* **50,** 1133–1147.

Eliassen, A., and M. Lystad, 1977: The Ekman layer of a circular vortex: A numerical and theoretical study. *Geophys. Norv.,* **31,** 1–16.

Emanuel, K., 1986: An air–sea interaction theory for tropical cyclones. Part I: Steady-state maintenance. *J. Atmos. Sci.,* **43,** 585–604.

——, 1988: Toward a general theory of hurricanes. *Amer. Sci.,* **76,** 370–379.

——, 1991: The theory of hurricanes. *Annu. Rev. Fluid Mech.,* **23,** 179–196.

Flatau, M., W. H. Schubert, and D. E. Stevens, 1994: The role of baroclinic processes in tropical cyclone motion: The influence of vertical tilt. *J. Atmos. Sci.,* **51,** 2589–2601.

Frank, W. M., and E. A. Ritchie, 1999: Effects of environmental flow upon tropical cyclone structure. *Mon. Wea. Rev.,* **127,** 2044–2061.

——, and ——, 2000: Effects of vertical shear on the structure and intensity of hurricanes. *Extended Abstracts, 24th Conf. on Hurricanes and Tropical Meteorology,* Fort Lauderdale, FL, Amer. Meteor. Soc., 5–6.

——, and ——, 2001: Effects of vertical wind shear on the intensity and structure of numerically simulated hurricanes. *Mon. Wea. Rev.,* **129,** 2249–2269.

Franklin, J. L., S. J. Lord, S. E. Feuer, and F. D. Marks, 1993: The kinematic structure of Hurricane Gloria (1985) determined from nested analyses of dropwinsonde and Doppler radar data. *Mon. Wea. Rev.,* **121,** 2433–2451.

Gamache, J. F., F. D. Marks, and F. Roux, 1995: Comparison of three airborne Doppler sampling techniques with airborne in situ wind observations in Hurricane Gustav (1990). *J. Atmos. Oceanic Technol.,* **12,** 171–181.

Gunn, R., and G. D. Kinser, 1949: The terminal velocity of fall for water droplets in stagnant air. *J. Meteor.,* **6,** 243–248.

Hildebrand, P. H., C. A. Walther, C. Frush, J. Testud, and F. Baudin, 1994: The ELDORA/ASTRAIA airborne Doppler weather radar goals, design, and first field test. *I.E.E.E. Trans. Geosci. Remote Sens.,* **82,** 1873–1890.

Holland, G. J., 1997: The maximum potential intensity of tropical cyclones. *J. Atmos. Sci.,* **54,** 2519–2541.

Hong, X., S. W. Chang, S. Raman, L. K. Shay, and R. Hodur, 2000: The interaction between Hurricane Opal (1995) and a warm core ring in the Gulf of Mexico. *Mon. Wea. Rev.,* **128,** 1347–1365.

Jones, S. C., 1995: The evolution of vortices in vertical shear. I: Initially barotropic vortices. *Quart. J. Roy. Meteor. Soc.,* **121,** 821–851.

Jorgensen, D. P., 1984a: Mesoscale and convective-scale characteristics of mature hurricanes. Part I: General observations by research aircraft. *J. Atmos. Sci.,* **41,** 1267–1285.

——, 1984b: Mesoscale and convective-scale characteristics of mature hurricanes. Part II: Inner core structure of Hurricane Allen (1980). *J. Atmos. Sci.,* **41,** 1287–1311.

——, P. H. Hildebrand, and C. L. Frush, 1983: Feasibility test of an airborne pulse Doppler radar. *J. Climate Appl. Meteor.,* **22,** 744–757.

——, E. J. Zipser, and M. A. LeMone, 1985: Vertical motions in intense hurricanes. *J. Atmos. Sci.,* **42,** 839–856.

——, T. Matejka, and J. D. DuGranrut, 1996: Multi-beam techniques for deriving wind fields from airborne Doppler radar. *J. Meteor. Atmos. Phys.,* **59,** 83–104.

Marks, F. D., Jr., 1985: Evolution of the structure of precipitation in Hurricane Allen (1980). *Mon. Wea. Rev.,* **113,** 909–930.

——, and ——, 1987: Inner core structure of Hurricane Alicia from airborne Doppler radar observations. *J. Atmos. Sci.,* **44,** 1296–1317.

——, R. A. Houze Jr., and John F. Gamache, 1992: Dual-aircraft investigation of the inner core of Hurricane Norbert. Part I: Kinematic structure. *J. Atmos. Sci.,* **49,** 919–942.

Molinari, J., S. Skubis, D. Vollaro, F. Alsheimer, and H. E. Willoughby, 1998: Potential vorticity analysis of tropical cyclone intensification. *J. Atmos. Sci.,* **55,** 2632–2644.

Montgomery, M. T., and R. Kallenbach, 1997: A theory for vortex-Rossby waves and its application to spiral bands and intensity changes in hurricanes. *Quart. J. Roy. Meteor. Soc.,* **123,** 435–465.

——, and J. Enagonio, 1998: Tropical cyclogenesis via convectively forced vortex Rossby waves in a three-dimensional quasigeostrophic model. *J. Atmos. Sci.,* **55,** 3176–3207.

Parrish, J. R., R. W. Burpee, F. D. Marks, and C. W. Landsea, 1984: Mesoscale and convective-scale characteristics of Hurricane Frederic during landfall. Postprints, *15th Conf. on Hurricanes and Tropical Meteorology,* Miami, FL, Amer. Meteor. Soc., 415–420.

Pasch, R. J., and M. Mayfield, 1996: Eastern North Pacific hurricane season of 1994. *Mon. Wea. Rev.,* **124,** 1579–1590.

Peng, M. S., B.-F. Jeng, and R. T. Williams, 1999: A numerical study of tropical cyclone intensification. Part I: Beta effect and mean flow effect. *J. Atmos. Sci.,* **56,** 1404–1423.

Rappaport, E. N., and M. Mayfield, 1992: Eastern North Pacific hurricane season of 1991. *Mon. Wea. Rev.,* **120,** 2697–2708.

Raymond, D. J., 1992: Nonlinear balance and potential-vorticity thinking at large Rossby number. *Quart. J. Roy. Meteor. Soc.,* **118,** 987–1015.

——, and H. Jiang, 1990: A theory of long-lived mesoscale convective systems. *J. Atmos. Sci.,* **47,** 3067–3077.

Reasor, P. D., M. T. Montgomery, F. D. Marks Jr., and J. F. Gamache, 2000: Low-wavenumber structure and evolution of the hurricane inner core observed by airborne dual-Doppler radar. *Mon. Wea. Rev.,* **128,** 1653–1680.

Reynolds, R. W., and T. M. Smith, 1994: Improved global sea surface temperature analyses using optimal interpolation. *J. Climate,* **7,** 929–948.

Schubert, W. H., and J. J. Hack, 1982: Inertial stability and tropical cyclone development. *J. Atmos. Sci.,* **39,** 1687–1697.

Shapiro, L. J., and H. E. Willoughby, 1982: The response of balanced hurricanes to local sources of heat and momentum. *J. Atmos. Sci.,* **39,** 378–394.

Shay, L. K., G. J. Goni, and P. G. Black, 2000: Effects of warm oceanic feature on Hurricane Opal. *Mon. Wea. Rev.,* **128,** 1366–1383.

Simpson, R. H., and H. Riehl, 1958: Mid-tropospheric ventilation as a constraint on hurricane development and maintenance. *Proc. Tech. Conf. on Hurruricanes,* Miami Beach, FL, Amer. Meteor. Soc. D4.1–D4.10.

Smith, R. K., 1981: The cyclostrophic adjustment of vortices with

application to tropical cyclone modification. *J. Atmos. Sci.,* **38,** 2021–2030.

Srivastava, R. C., 1987: A model of intense downdrafts driven by melting and evaporation of precipitation. *J. Atmos. Sci.,* **44,** 1752–1773.

Tuleya, R. E., and Y. Kurihara, 1981: A numerical study on the effects of environmental flow on tropical storm genesis. *Mon. Wea. Rev.,* **109,** 2487–2506.

Wang, Y., 2002: Vortex Rossby waves in a numerically simulated tropical cyclone. Part I: Overall structure, potential vorticity, and kinetic energy budgets. *J. Atmos. Sci.,* **59,** 1213–1238.

Willoughby, H. E., 1990: Temporal changes in the primary circulation in tropical cyclones. *J. Atmos. Sci.,* **47,** 242–264.

——, 1992: Linear motion of a shallow-water barotropic vortex as an initial-value problem. *J. Atmos. Sci.,* **49,** 2015–2031.

——, 1998: Tropical cyclone eye thermodynamics. *Mon. Wea. Rev.,* **126,** 3053–3067.

——, and M. B. Chelmow, 1982: Objective determination of hurricane tracks from aircraft observations. *Mon. Wea. Rev.,* **110,** 1298–1305.

——, J. A. Clos, and M. G. Shoreibah, 1982: Concentric eye walls, secondary wind maxima, and the evolution of the hurricane vortex. *J. Atmos. Sci.,* **39,** 395–411.

——, F. D. Marks, and R. J. Feinberg, 1984: Stationary and moving convective bands in hurricanes. *J. Atmos. Sci.,* **41,** 3189–3211.

Wu, C.-C., and K. A. Emanuel, 1993: Interaction of a baroclinic vortex with background shear: Application to hurricane movement. *J. Atmos. Sci.,* **50,** 265–274.

Zehr, R. M., 1992: Tropical cylogenesis in the western North Pacific. NOAA Tech Rep. NESDIS 61, 181 pp.